scientific reports

Check for updates

OPEN

Hydrogen isotopes retention studies using laser and microwave induced plasma coupling

N. Vujadinovic[1], I. Traparic[1], B. D. Stankov[1], D. Rankovic[2,3], M. Kuzmanovic[2] & M. Ivkovic[1]✉

The detection of deuterium and tritium retention in fusion devices via optical emission spectroscopy (OES) faces significant challenges due to experimental limitations, particularly in resolving hydrogen isotope Balmer alpha lines (H_α, D_α, and T_α). In this study, we propose and evaluate the coupling of laser ablation and laser-induced desorption with microwave-induced plasma (MIP) as an approach to resolve this problem. This approach effectively meets the resolution requirements for Balmer alpha lines, overcoming limitations of standard laser-induced breakdown spectroscopy (LIBS) setups. Optimization of Nd:YAG laser ablation was performed using pure copper and tungsten targets, while desorption, including femtosecond (fs) laser-induced desorption, was studied on graphite powder mixed with heavy water and water. The results demonstrate a significant improvement in spectral resolution and analytical performances, highlighting the potential of this technique for tritium retention studies in plasma-facing components.

Keywords Hydrogen isotopes retention, Laser ablation, Laser induced desorption, Microwave induced plasma, Plasma-facing components, LIBS

Diagnostics of the fusion plasma reactors are critical for ensuring their safe and proper stable operation. Among these diagnostics, the hydrogen isotope retention, particularly tritium, in plasma facing components (PFC) are probably the most important ones[1]. Techniques such as ion beam analysis (IBA) and thermal desorption spectroscopy studies (TDS) are highly reliable and commonly used PFC diagnostics methods[2–5]. However, these methods are constrained to laboratory settings and require complex equipment. Consequently, sections of the PFC or test targets positioned on various places within the vacuum vessel must be demounted from the reactor wall[6] to be analyzed.

To enable in-situ analysis of PFC, laser induced breakdown spectroscopy (LIBS) is used as an effective solution to overcome limitations of traditional methods. LIBS is a minimally invasive, non-contact technique suitable for multi-element analysis, including depth profiling, without requiring sample preparation. The technique is adaptable for vacuum or low-pressure gas environments and has been applied across diverse fields, such as nitrogen detection in soil[7], explosives detection[8], olive oil classification[9], cadmium detection in drinking water[10], and even the identification of malaria biomarkers[11], bacteria[12] or SARS[13]. LIBS is also commonly used for analyzing metal purity, alloys, jewelry[14], archaeological and other samples. Reviews[15–18] and recent studies[19–21] provide comprehensive insights into the advancements of LIBS for fusion applications, particularly its potential for in-situ diagnostics.

The most important application of LIBS for plasma fusion reactor wall diagnostics is the study of hydrogen isotope retention, which relies on measurement of their Balmer alpha spectral lines. A significant challenge in this application is resolving the closely spaced lines caused by the small isotope shift. Even high-resolution spectrometers struggle to resolve these lines, due to significant Stark broadening under standard LIBS plasma conditions[22]. Partial resolving of a hydrogen and deuterium Balmer alpha lines (with isotope shift of 0.18 nm) has been achieved in studies using double-pulsed LIBS, where line fitting with a Voigt function was employed[17,23,24]. More recently, approaches based on femtosecond (fs) laser ablation[25] and fs LIBS[26] have been applied to hydrogen isotope retention diagnostics, demonstrating further advancements in this field[27–32].

The use of the TEA CO_2 lasers or Nd:YAG in He[33–35] or filament fs laser LIBS[27,30] demonstrates the possibility of LIBS to resolve H_α and D_α lines. However, resolving T_α lines presents a greater challenge due to the stricter requirements for low electron density[22]. In this study, we propose overcoming these challenges by coupling laser and microwave-induced plasma (MIP) to achieve the necessary plasma conditions. Two sample introduction

[1]Institute of Physics, University of Belgrade, 11080 Belgrade, Serbia. [2]Faculty of Physical Chemistry, University of Belgrade, 11158 Belgrade, Serbia. [3]Present address: Vinca Institute of Nuclear Science, University of Belgrade, 11000 Belgrade, Serbia. ✉email: ivke@ipb.ac.rs

methods are employed: laser ablation using an Nd:YAG laser and fs laser-induced desorption, both integrated with microwave-induced low-pressure plasma.

Experiment

Microwave induced plasma is the primary method used in this research for excitation and resolution of hydrogen isotope lines. The combination of MIP and laser induced plasma was used earlier for the enhancement of the LIBS[36,37], where the addition of microwaves increased electron density, temperature, and plasma duration and dimensions. However, this enhancement also increased Stark broadening, making the method unsuitable for tritium retention studies. In contrast, MIP source operating at atmospheric pressure has plasma parameters[38,39] suitable for resolving D_α and T_α spectral lines, as analyzed in[22]. At low gas pressures, MIP achieves even smaller electron densities[40], minimizing Stark and Van der Waals broadening, making them negligible in comparison with other broadening mechanisms (Doppler and instrumental). For this study, a Beenakker resonator cavity with an 8 mm diameter and 14 cm long capillary tube was used, with an optical window and evacuation port mounted at the end. MIP was generated using an AHF Analysen Technik GMW 24–301 DR 2.45 GHz microwave generator with a maximum power of 100 W. A double gauge gas regulator and needle valve regulated gas flow withing the tube. Gas pressure was measured with a manometer, and a mechanical vacuum pump was used for evacuation and maintaining stable argon gas flow.

The first method used for sample introduction was laser ablation, a widely used technique in analytical spectroscopy for introducing samples into excitation sources such as inductively coupled plasma (ICP), MIP, LIBS or mass spectrometry[41–43]. For this purpose, we used a laboratory made laser ablation cell, see Fig. 1. This cell was constructed as an elongation of the capillary tube thus enabling the most efficient transport of the ablated material into the MIP. The target was placed in a custom built holder with vacuum feedthrough, allowing rotation to expose fresh target surface area to the laser beam. Ablation was performed using Quantel 450 Nd:YAG (1064 nm, 6 ns pulse duration, 10 Hz maximum repetition rate, 450 mJ maximum energy). Laser beam was focused with a f= 12.5 cm lens through the window and onto the target. Special cell design enables irradiation of the target at approximately 45 degrees. Small variation of incident angle enables irradiation at a variable distance from the center of the target. That way, laser induced plasma radiation, which always propagates normal to the target surface, does not reach detection system and enables recording of the radiation coming from the MIP only.

The emitted light from the MIP was collected through an optical window at the end of the capillary using a collimator (COLL) and guided via fiber optic cable (OF) either to medium resolution spectrometer Andor Shamrock 303i (with grating 1200 g/mm) or high-resolution spectrometer SOL instruments MS7504i spectrometer (with grating 1800 g/mm). The Andor spectrometer was equipped with Andor iStar DH720 - 18 F-63 ICCD camera (256 × 1024 pixels, 26 μm pixel size), while SOL instruments spectrometer was equipped with Andor iStar DH734 - 18 F- 63 ICCD camera (1024 × 1024 pixels, 13 μm pixel size), that were used as detectors. Delay and gating of cameras were controlled with external digital delay generator (DDG, Stanford Research SRS 535), which was triggered with the signal for opening of a Nd:YAG laser Q switch. It should be noted that the

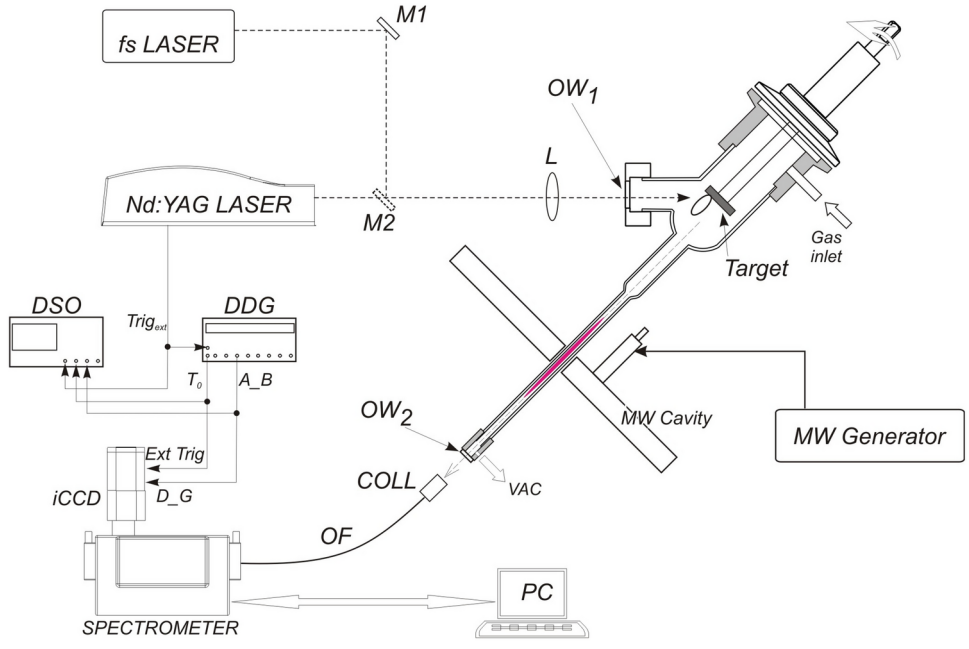

Fig. 1. Experimental setup for laser ablation (using Nd:YAG) and laser induced desorption (using fs Yb:YAG laser) as methods for sample introduction in microwave induced plasma (MIP). DSO—digital storage oscilloscope, DDG—digital delay generator, COLL—collimator of the emitted radiation into the fiber, OF—optical fiber, M—folding mirrors, VAC—vacuuming port, L—focusing lens, OW—optical windows.

separation of the optical emission signals created by LIBS and by MIP can also be achieved by changing the delay and gate time of the camera exposure.

The Nd:YAG laser, commonly used for plasma creation, is known to ablate a thick layer of material, making it unsuitable for analyzing thin films or surface-bound elements. For detecting hydrogen isotopes within thin surface layers, laser-induced desorption (LID)[44–46], often paired with quadrupole mass spectrometry (LID-QMS)[47], is a more suitable approach. To test the feasibility of using MIP as an alternative to the more complex QMS, a femtosecond Yb:YAG laser (Solar FX200, 1030 nm, 150 fs pulse duration, 105 nJ peak energy, 71 MHz repetition rate, 7 W average power) was employed for laser-induced desorption of hydrogen isotopes. In this setup, the detection system was triggered by the camera's internal trigger with a variable exposure time. While this study utilized the femtosecond laser, laser-induced desorption can also be achieved with other lasers capable of heating the target without causing significant ablation.

The selected targets for these studies included a copper target for the experiment optimization in terms of gas pressure, delay time, microwave power and laser energy. A tungsten target was then introduced to verify the optimized conditions for resolving Balmer alpha spectral lines. Finally, a pill composed of graphite powder mixed with water and heavy water (D_2O), was prepared using a hydraulic press, as previously described in[22]. This pill was tested for both laser-induced desorption and vacuum-induced desorption.

Results

In the investigation of MIP for hydrogen isotope detection, the initial task involved optimizing the transport and excitation of sample components. Due to the challenges associated with tritium's radioactivity, most previous research has focused on deuterated samples as a safer alternative. In this study, tungsten (W) samples containing incorporated deuterium were analyzed using laser ablation as the method for introducing samples into the MIP.

Laser ablation

The investigation of Nd:YAG laser ablation as a method for introducing tungsten samples with incorporated deuterium into the MIP proved nearly impossible with our experimental setup. This was due to several factors: The high reflectivity of the polished samples, the shallow retention of the deuterium and high laser ablation rate. As a result, the application of MIP for hydrogen isotopes detection using laser ablation was limited to optimizing parameters for resolving hydrogen isotope Balmer alpha lines. According to[22], D_α and T_α spectral lines can be resolved only if full width at half maximum (FWHM) of lines is less than 0.056 or even 0.027 nm, depending on their intensity ratio (1:1 or 1:10, respectively). Furthermore, FWHMs of the neighbor spectral lines must also be smaller than the wavelength separation between them and hydrogen isotope lines.

To obtain the best resolving results, using laser ablation, the signal to noise ratio (i.e., line intensities) has to be maximized by optimizing several experimental parameters, while keeping FWHM as minimal as possible. For MIP operation, microwave power and gas pressure are the most important parameters. The line intensities increase with microwave power, but the reflected power also increases. If the reflected power exceeds 15 W, there is a risk of damaging the microwave generator or overheating the discharge tube. Optimal gas pressure, which corresponds to the flow rate, must also be determined, as it dictates the time the sample remains within the MIP resonator cavity for excitation.

Additionally, the dependence of spectral line intensities on laser energy was analyzed, as laser energy influences the ablation process, specifically the ablated mass and particle dimensions. Although higher energy increases the ablated mass, it is important to assess whether larger particle dimensions might affect MIP performance by altering microwave coupling to the plasma or causing particle deposition on the tube walls.

Optimization of gas pressure

The optimal gas pressure range for stable MIP operation was determined by analyzing the maximal intensity of the Ar I line at 516.22 nm ($3s^23p^5(^2P^0{}_3/_2)4p \rightarrow 3s^23p^5(^2P^0{}_3/_2)6d$), as shown in Fig. 2a. The Ar I line was used to establish the optimal gas pressure range since its intensity is independent of the camera recording delay. In contrast, the intensities of the target lines, such as Cu I, depend on the gas flow rate, which determines when the ablated material reaches the plasma.

From Fig. 2b, the optimal gas pressure range for stable MIP operation was between 15 and 20 mbar.

The optimal gas pressure can be determined using the most intense spectral line, the Cu I line at 521.82 nm ($3d^{10}4p \rightarrow 3d^{10}4d$). Since this line is susceptible to self-absorption, its optical thickness was evaluated. The Cu I lines at 515.32 nm (λ_1) and 521.82 nm (λ_2) belong to the same multiplet (transition $3d^{10}4p \rightarrow 3d^{10}4d$) as shown in Fig. 2a. To assess self-absorption of the 521.82 nm line, the intensity ratio $R = I_{\lambda 1}/I_{\lambda 2}$ was compared at various pressures to the theoretical value of $R = 0.53$ (Table 1)[48]. Results indicated no significant self-absorption for all pressures except at 10 mbar, where the lines exhibited low intensity.

Since the Cu I line has a significantly higher intensity at 20 mbar, see Fig. 2b, this line was used in optimization of several experimental parameters in all further investigations.

Optimization of material transport to the MIP

Gas pressure and flow regulate the duration for which the ablated material remains in the discharge, thereby influencing the recording parameters (delay and gate times). The delay corresponds to the time required for the material to travel from the target to the resonator cavity, while the gate time determines the duration the material spends in the discharge zone. An analysis of the optimal delay time is presented in Fig. 3. It should be noted that for this and all further analyses the gate was fixed to 10 ms.

Based on Fig. 3 it was concluded that the delay time should be 20 ms and that the 10 ms gate time is appropriate. During these measurements, microwave power was set to 75 W and laser energy was 250 mJ. The final spectrum was the accumulated spectrum of 20 laser shots.

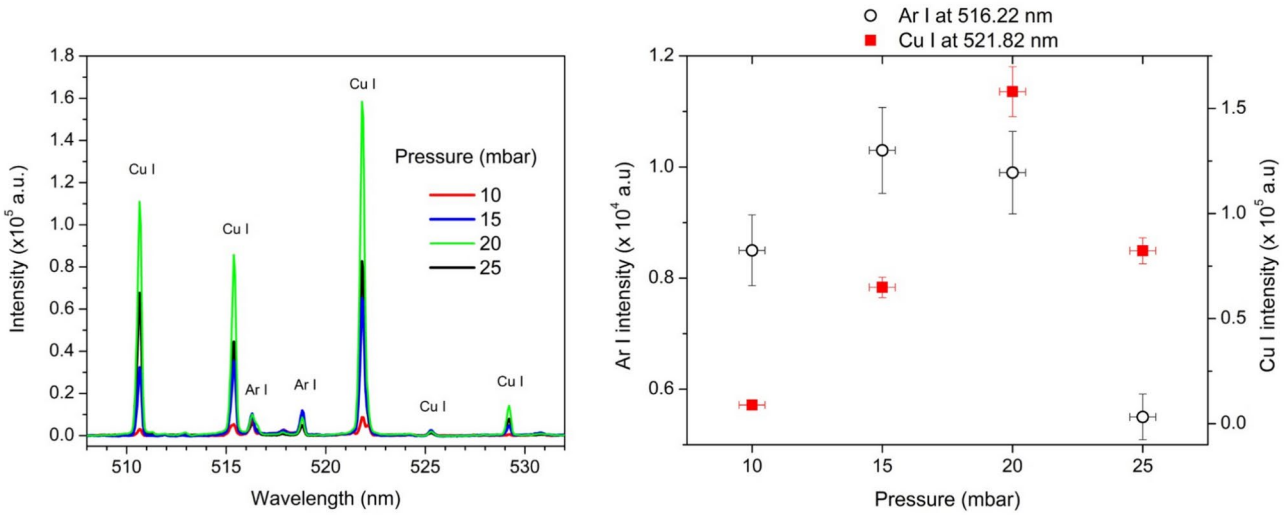

Fig. 2. (**a**) MIP spectra of a laser-ablated Cu target in Ar at various pressures. Experimental parameters: MIP power: 75 W, delay: 8 ms, gate: 10 ms, number of accumulations: 20. (**b**) Selected Ar and Cu line intensities as a function of pressure.

Pressure (mbar)	$R = I_{\lambda 1}/I_{\lambda 2}$ (exp.)
10	0.66
15	0.54
20	0.53
25	0.54

Table 1. Experimental ratios of the intensities of Cu I spectral lines at various pressures.

Optimization of ablated material quantity

The amount of ablated material is directly influenced by the laser energy used. To optimize this parameter, the laser energy was adjusted by varying the delay between the triggering of the flash lamps and the opening of the laser Q switch (FLQS). Three energy values were tested: 130, 250 and 430 mJ. The resulting graph is shown in Fig. 4.

With the increase of the laser energy, the intensity of the Cu I line also increases. This is primarily due to the ablation rate, as when the energy of the laser is higher, the ablation rate is also higher, and more material is entering the discharge region. Here, the energy of 250 mJ was chosen, as for the higher energy, the mass of the incoming material was too large, which caused the MIP discharge to shut down.

Selection of microwave generator power

Dependence of the line intensity on the microwave power supplied to the cavity (for optimal pressure, delay, gate and laser energy) was analyzed. Here, four powers were considered (50, 60, 75 and 90 W). Besides supplied power, the reflected power was also measured. The obtained dependance on the supplied power is shown in Fig. 5.

The results indicate that increasing the supplied power leads to a corresponding increase in line intensity. However, the reflected power also rises with higher input power. In Fig. 5, a dashed vertical line marks the input power at which the reflected power reaches 15 W. Since exceeding this threshold could overheat the source, it is not advisable to operate beyond this limit. Consequently, 75 W was selected as the optimal power setting to ensure safe and reliable generator operation.

Spectral resolution requirements for hydrogen isotopes retention studies

After optimizing experimental parameters for laser ablation and MIP operation the potential of this setup for hydrogen isotopes retention studies was analyzed. For such analysis, the FWHM of Balmer alpha lines should be less than 0.027 nm if one wants to detect small amounts of tritium in the first wall of future fusion reactors. The first step in this direction was to assess the instrument broadening on the spectral lines' widths. Given the negligible Stark broadening at low MIP gas pressures ($Ne \sim 10^{12}$ cm^{-3}), and the electron temperature between 2000 and 3000 K, we can safely assume that the major influence in the line broadening comes from the Doppler and instrument broadening. To determine the instrumental FWHM of device, the recorded Cu I line at 521.82 nm from Fig. 2 was fitted with a Gaussian function. The resulting FWHM was 0.27 nm, which greatly exceeds the goal of having lines as narrow as 0.027 nm. This result is reasonable, considering that medium resolution

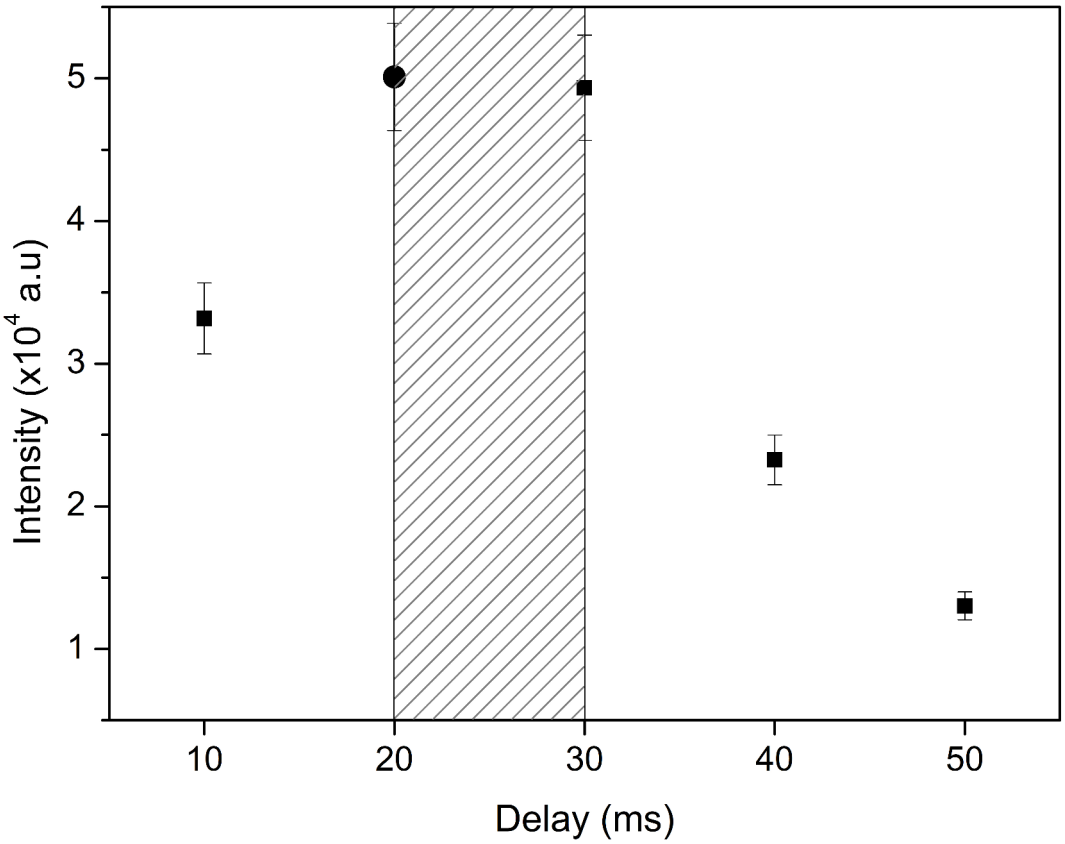

Fig. 3. Optimization of the delay time between the laser pulse and camera triggering by maximizing intensity of the 521.82 nm Cu I line. Shaded area represents the gate time.

Shamrock 303 imaging spectrograph with the entrance slit width of 50 µm equipped with Andor iStar DH720 ICCD camera was used for these measurements.

To reduce the instrumental broadening of the lines, the high resolution MS7504i spectrometer with the entrance slit width of 30 µm equipped with Andor iStar DH734 - 18 F- 63 ICCD camera was used for recording spectral lines of tungsten. As part of the optimization of the optical system (selection of the spectrometer and slit width), W target was used to verify whether the W line FWHM is less than 0.04 nm, which corresponds to the wavelength separation between hydrogen Balmer alpha line at 656.28 nm and W I line at 656.32 nm.

Gaussian fitting of the W I lines (Fig. 6) showed the FWHM of 0.024 nm at 429.46 nm and 0.025 nm at 430.21 nm, meeting the required resolution. This demonstrates that the setup is capable of enabling precise determination of the H_α line intensity.

Desorption as a method for sample introduction in MIP

To obtain the H_α and D_α FWHM values and to test whether resolving the D_α and T_α lines is possible in this configuration, and for previously determined optimal experimental parameters of 20 ms delay and 10 ms gate time, 75 W MIP input power and a 30 µm entrance slit width of the high resolution spectrometer, a mixture of graphite powder, heavy water and water, pressed into a pill, was used as the target. In section"Desorption due to vacuuming", the results of the MIP spectrum for desorption induced by the vacuuming alone are presented, while in section"Laser induced desorption", the results of desorption induced by fs laser heating in combination with the vacuum pump are presented.

Desorption due to vacuuming

Due to the composition of the target pill, water and heavy water were not fully bonded to the graphite, resulting in their evaporation from the target during vacuum pump outgassing. The corresponding MIP spectra with deuterium and hydrogen Balmer alpha lines is shown in Fig. 7. As can be seen, the lines are narrow and fully resolved.

Laser induced desorption

As a final step, we examined whether a 1030 nm fs laser with very low energy (100 nJ) could induce desorption of hydrogen isotopes from the target and introduce them into MIP. Two cycles of heating were performed and recorded. During target heating, an increase in the D_α and H_α line intensities was observed, without a corresponding increase in their FWHMs. MIP spectra, after turning off the laser following the second heating cycle, is shown in Fig. 8. The effect of laser induced desorption is evident: During the cooling of the target, the

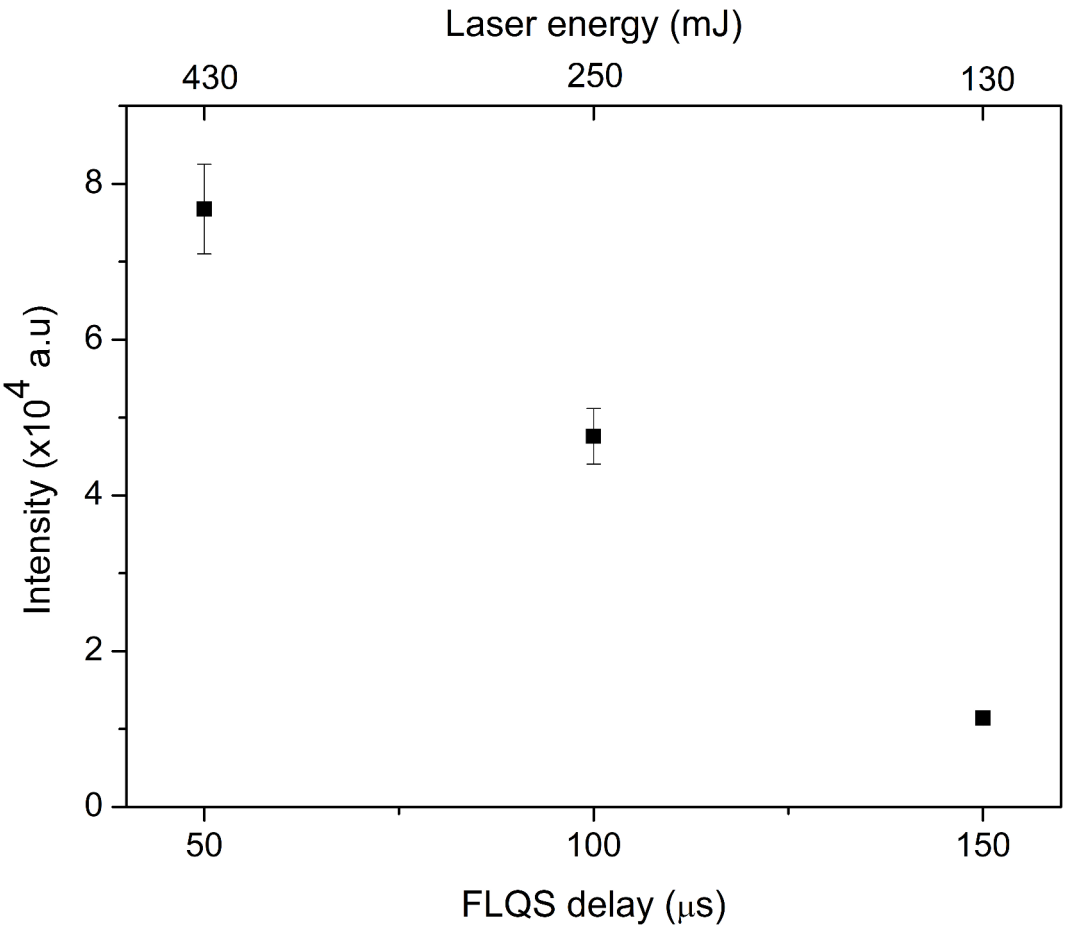

Fig. 4. Dependence of the 521.82 nm Cu I line intensity on the laser energy controlled with FLQS delay, for the optimal pressure, delay and gate time.

line intensities gradually decrease to the levels seen in Fig. 7, where desorption was induced by the vacuum pump alone.

As can be noted from Figs. 7 and 8 (6 min after), the ratio of D_α and H_α peaks remained the same after laser irradiation, but for other measurements that ratio varies. The target was made with equal shares of D_2O (> 99% purity) and H_2O, but there is additional contribution to the H_α peak that comes from the desorption of water vapor from the walls of the discharge tube. The time dependency of the D_α line intensity during both cycles is shown in Fig. 9. The effects of laser heating and laser induced desorption are clear. The intensity increased while the laser was active, peaking at the moments when the laser was turned off. After that, intensity decreased gradually. This confirms that the deuterium comes from laser induced desorption, rather than solely from outgassing due to the vacuum pump. It should be noted that the intensity from the first measurement is higher than it should be, because not enough time has passed for the target to cool from the previous test measurements. The starting value should be close to the one shown in Fig. 7, as that was recorded before the laser heating.

Before proceeding to the estimation of hydrogen isotope line widths, plasma parameters were estimated. The excitation temperature was estimated from the Boltzmann plot of Ar I lines to be 2600 K. Boltzmann plot is given in Fig. 10. Complete data for the lines used to obtain the Boltzmann plot can be found in the Supplementary Table S1.

Given the expected low electron density and negligible Stark broadening for both hydrogen and argon lines, an attempt was made to estimate the upper limit for electron density. The merging of spectral lines of hydrogen is a suitable method for this estimation. If the final detectable spectral line of Balmer series is found, then the use of Inglis – Teller relation[49] can give the upper limit on the electron density. The final observed member of the Balmer series in this study was H-η (9 → 2, 383.5 nm), shown in Fig. 11. Assuming $N_e = N_i$, and that for hydrogen atoms the effective nuclear charge (z) is 1, the upper limit of electron density $Ne \sim 6.3 \cdot 10^{15}$ cm^{-3} was obtained. This value is a huge overestimation, since the upper members of the series couldn't be detected due to the presence of different molecular bands. For precise resolution of superimposed signals, whether due to electric noise or molecular bands, more detailed measurements with even higher spectral resolution would need to be conducted. Regarding Balmer alpha lines, molecular bands close to them have negligible intensities, if they are present at all, and they have no influence on $H_\alpha/D_\alpha/T_\alpha$ intensity ratio.

$$\log(N_e + N_i) = 23.26 - 7.5\log n_{max} + 4.5\log z \quad (1)$$

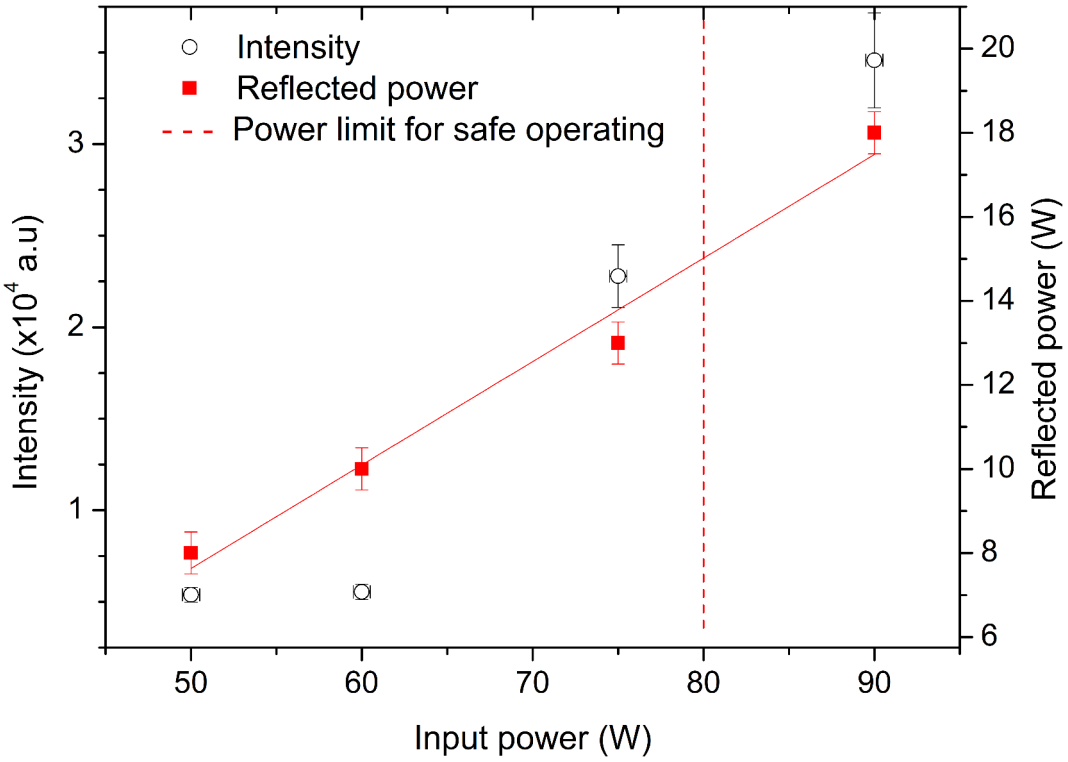

Fig. 5. Intensity of the 521.82 nm Cu I line and microwave generator reflected power as a function of microwave generator input power.

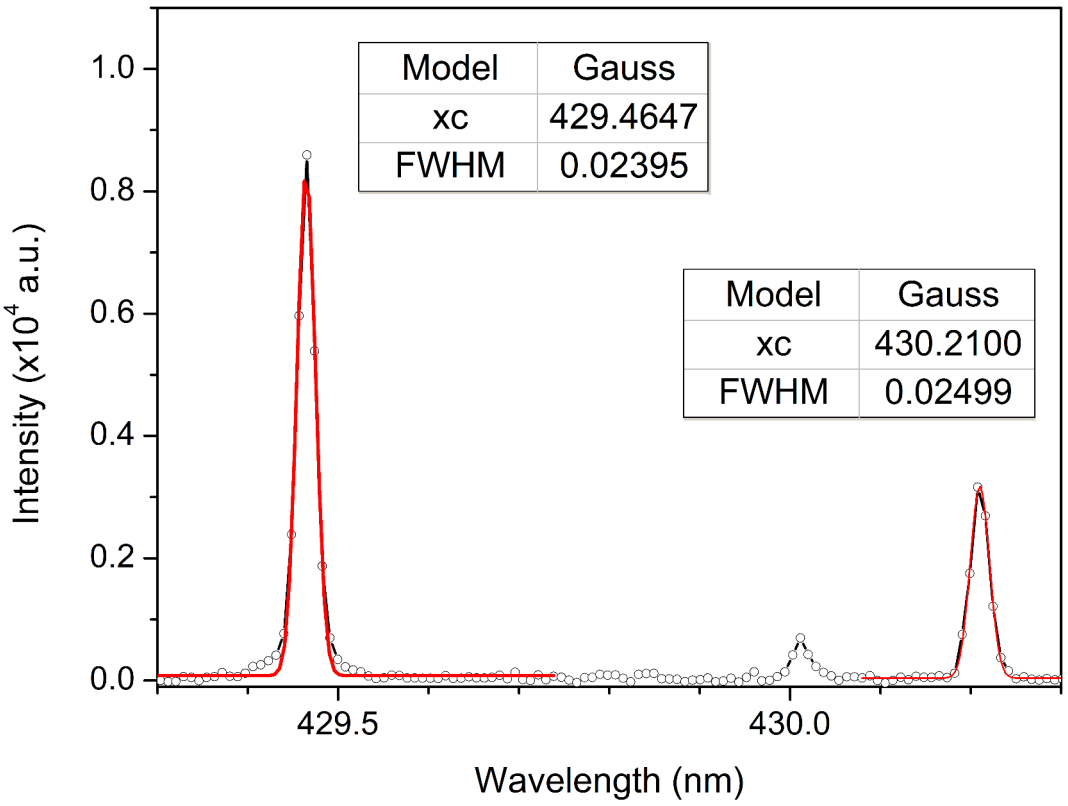

Fig. 6. Gaussian fit of W I lines recorded with high resolution spectrometer with a 30 μm entrance slit width.

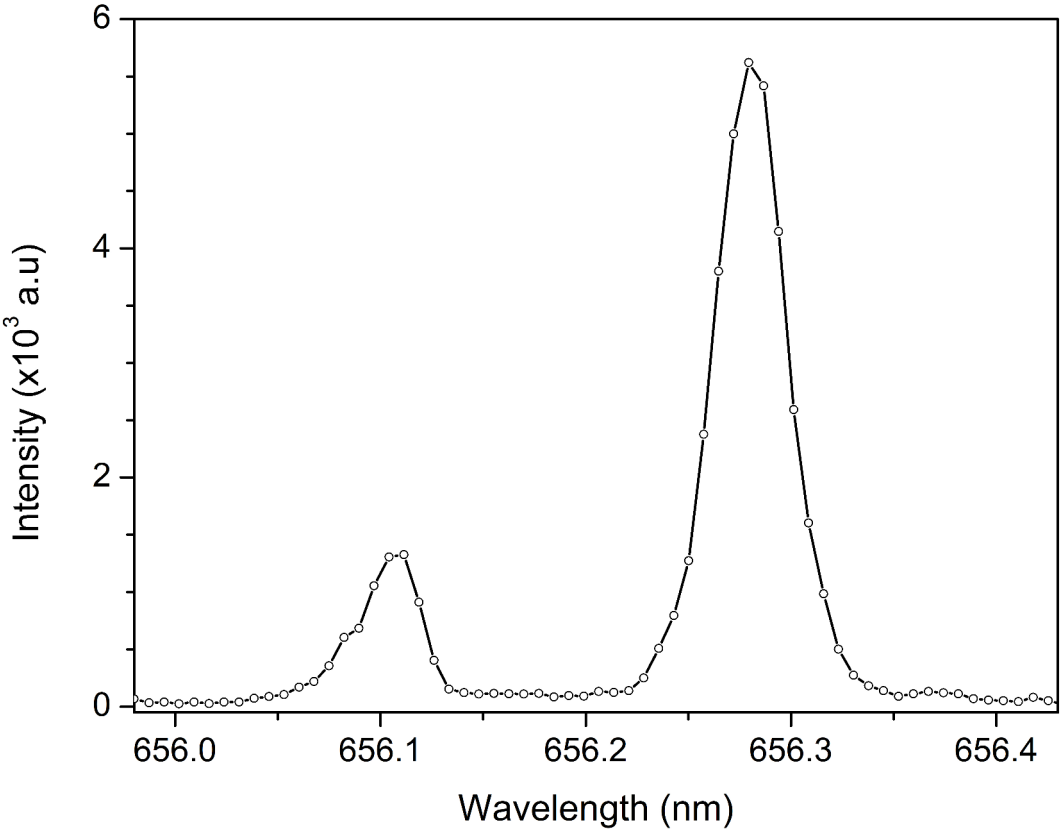

Fig. 7. D_α and H_α lines from MIP when the vacuum pump is the sole contributor to the sample's desorption.

Another approach for determining the electron density is through the Stark broadening of the upper members of the Balmer series. Since the highest detected member of the Balmer series has the width close to the instrumental width, and considering the errors during the fitting procedure, it can be estimated that the Stark width of the Balmer alpha lines doesn't exceed 0.01 nm. If this value is inserted into the formula for the estimation of line widths from the higher members of the Balmer series[50]

$$N_e = 8 \cdot 10^{18} \cdot \left(\frac{w_S\,(nm)}{\alpha^n_{1/2}} \right)^{1.5} \tag{2}$$

the resulting value, with $\alpha^n{}_{1/2} = 0.345$ (for $n = 9$), would be $N_e = 1.25 \cdot 10^{12}$ cm^{-3}, which is a more realistic estimation than the one obtained by the Inglis – Teller equation.

Finally, to confirm the necessary resolution for the hydrogen retention studies, both lines were fitted with a Voigt profile (Fig. 12). Gaussian fitting was also attempted, but Voigt profile showed better performance in terms of wing fitting.

Approximative equation for Voigt profile FWHM[51]

$$W_V \approx 0.5346 W_L + \sqrt{0.2166 W_L^2 + W_G^2} \tag{3}$$

was used with coefficients obtained from Fig. 12. The resulting line widths are 0.033 nm for D_α line and 0.038 nm H_α line. Although Voigt line widths are correct, the Gaussian and Lorentzian parts are off. Gaussian parts can be calculated using the equation

$$W_G = \sqrt{(W_D^2 + W_I^2)}, \tag{4}$$

where W_D represents the Doppler line width and W_I is the instrumental line width. Doppler broadening FWHM can be calculated using the equation

$$W_D = 7.16 * 10^{-7} \lambda \sqrt{\frac{T}{M}}, \tag{5}$$

where M is the mass of the emitter, given in atomic mass units, and T is the temperature estimated using a Boltzmann plot of the Ar I lines (Fig. 10). Since the instrumental FWHM was estimated at 0.024 nm, based on

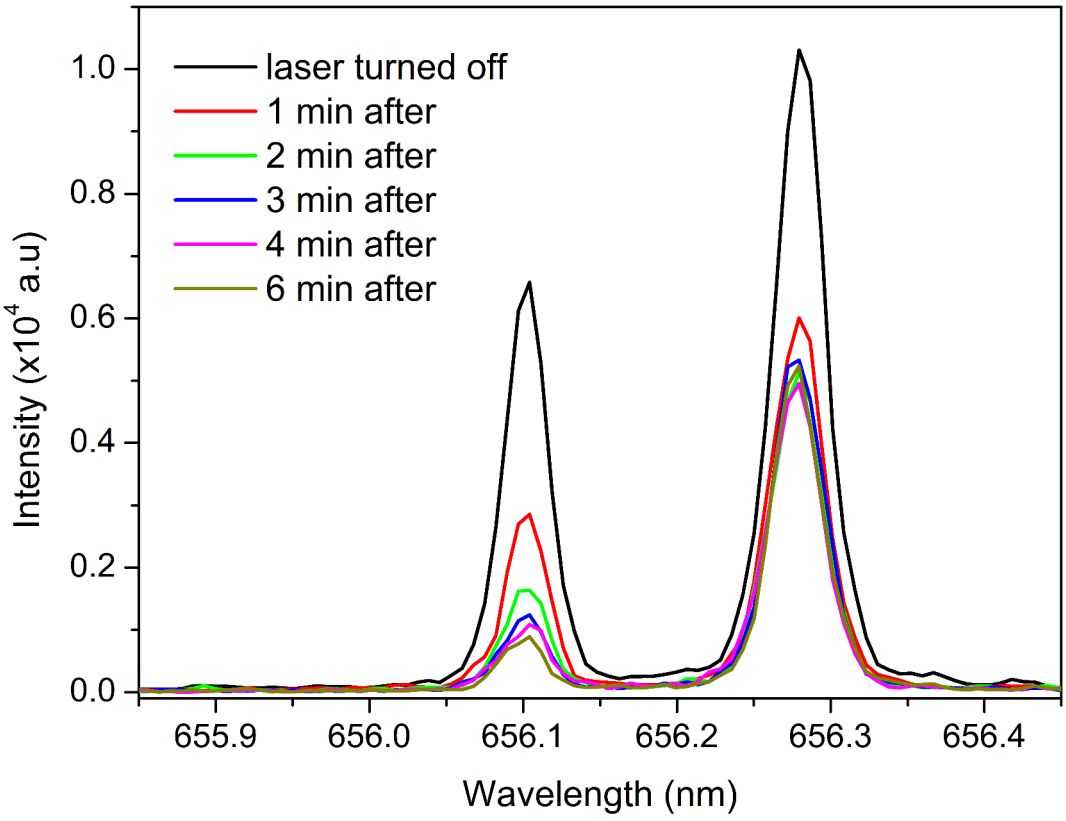

Fig. 8. D_α and H_α line intensities after heating the target with the fs laser in the second cycle.

FWHM of W I 429.46 nm line from Fig. 6, Gaussian parts of the Voigt profiles are 0.029 nm and 0.034 nm for D_α and H_α, respectively. Lorentzian parts are then calculated using the Eq. (3), and they are 0.007 nm for both D_α and H_α.

Finally, using the formula suggested in[22], the intensity ratio of T_α and D_α for which both lines could be resolved was obtained. The critical FWHM at which mentioned lines can be resolved relates to the intensity ratio $R = T_\alpha/D_\alpha$ through the following formula[22]:

$$FWHM_{cr} = 0.0599 - 0.0388 \times e^{-1.765 \times R} \tag{6}$$

Now, for the determined FWHM of D_α 0.033 nm, the theoretical ratio of lines is $R = 0.2$. Therefore, our proposed method could resolve D_α and T_α lines up to the point where D_α is five times more intense than T_α, or vice versa.

Conclusion

In this work, we explored the coupling of laser-induced desorption and laser ablation with microwave-induced plasma as an effective method for studying hydrogen isotope retention in plasma-facing components of fusion devices. The experimental setup was optimized to achieve high spectral resolution, demonstrating great separation of hydrogen and deuterium Balmer alpha lines, which would theoretically enable the separation of deuterium and tritium Balmer alpha lines up to the point where D_α is five times more intense than T_α, or vice versa. The application of femtosecond laser for desorption facilitated sample introduction into the MIP, as evidenced by the clear enhancement of the D_α line. Under low-pressure MIP conditions, line broadening effects were minimized, enabling precise isotopic analysis. It should be stressed that stoichiometry problem[52], i.e., whether the H/D ratio in the plasma corresponds to the H/D ratio in the target is under study.

This study presents a significant advancement in the diagnostics of tritium retention, offering a minimally invasive, high-resolution approach that addresses the limitations of traditional methods such as ion beam analysis and thermal desorption spectroscopy. The findings underscore the potential of this technique for in-situ applications in fusion research, contributing to the development of safer and more efficient plasma diagnostics systems. Future work will focus on scaling this approach for broader fusion reactor applications and extending it to analyze mixed material deposits.

Currently, this approach is suitable for post-mortem analysis (between experimental campaigns). The authors are working on a measuring device that will enable the application of this method for real-time in situ measurements (without demounting the components in tokamak).

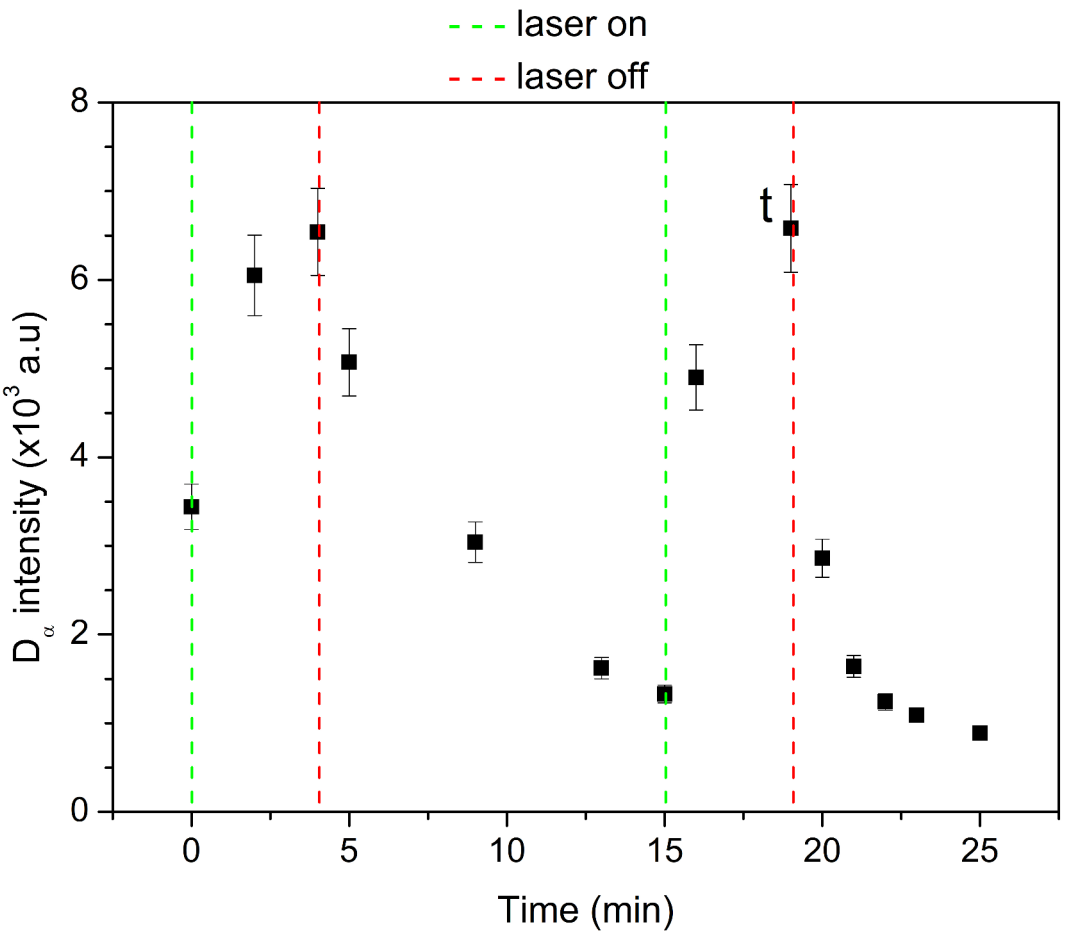

Fig. 9. Time evolution of the D_α line intensity during two cycles of heating and cooling of the target.

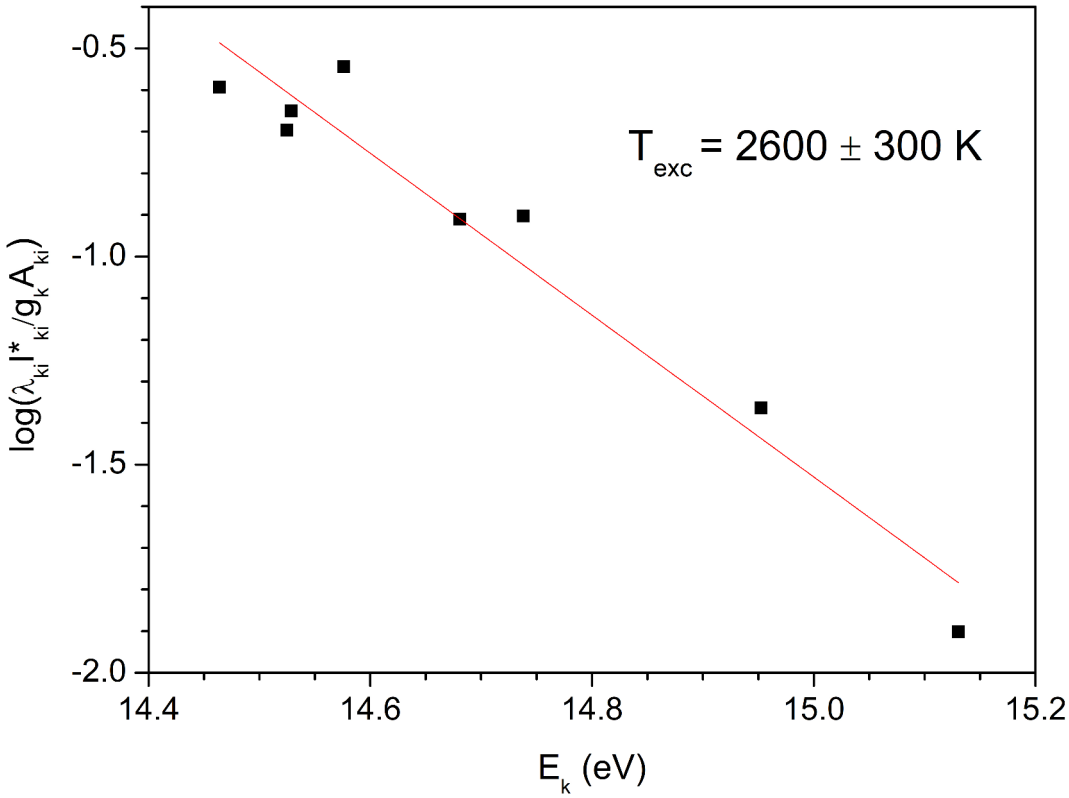

Fig. 10. Boltzmann plot of the Ar I lines for excitation temperature estimation.

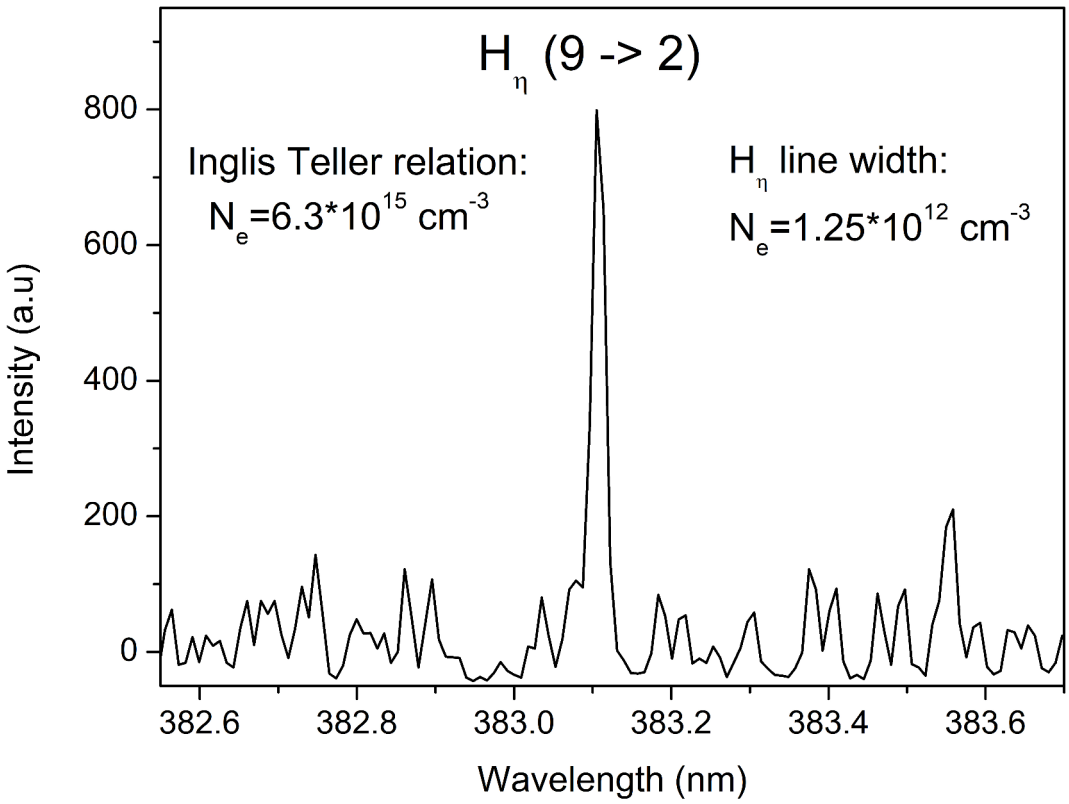

Fig. 11. Balmer Hη line at 383.5 nm recorded for estimation of electron density.

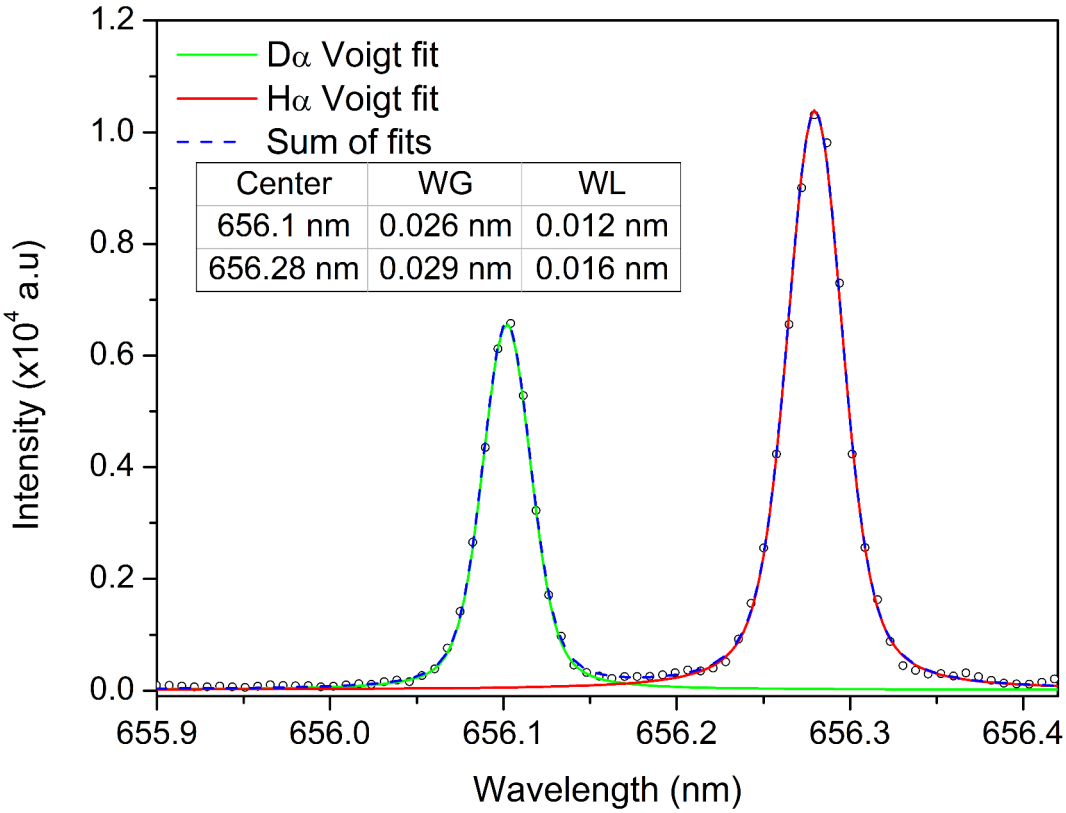

Fig. 12. Voigt profile fitting of the D_α and H_α lines for the measurement at time t, marked in Fig. 9.

Data availability

The data that supports the findings of this study is available from the corresponding author upon reasonable request.

Received: 27 January 2025; Accepted: 28 March 2025
Published online: 12 April 2025

References

1. Brezinsek, S. et al. Fuel Retention Studies with the ITER-like Wall in JET. *Nucl. Fusion* **53**, 083023 (2013).
2. Rubel, M. et al. The role and application of ion beam analysis for studies of plasma-facing components in controlled fusion devices. *Nucl. Instrum. Method. Phys. Res. Sect. B.* **371**(4), 11 (2016).
3. Mayer, M. et al. Ion beam analysis of fusion plasma-facing materials and components: Facilities and research challenges. *Nucl. Fusion* **60**, 025001 (2020).
4. Oya, Y. et al. Development of H, D, T simultaneous TDS measurement system and H, D, T retention behavior for DT Gas exposed tungsten installed in LHD plasma campaign. *Fusion Sci. Technol.* **71**, 351–356 (2017).
5. Oya, Y. et al. Effect of impurity deposition layer formation on D retention in LHD plasma exposed W. *Nucl. Mater. Energy* **9**, 84–88 (2016).
6. Alimov, VKh., Yajima, M., Masuzaki, S., Tokitani, M., LHD Experiment Group. Analysis of mixed-material layers deposited on the toroidal array probes during the FY 2012 LHD plasma campaign. *Fusion Eng. Des.* **147**, 111228 (2019).
7. Hossen, M. A., Diwakar, P. K. & Ragi, S. Total nitrogen estimation in agricultural soils via aerial multispectral imaging and LIBS. *Sci. Rep.* **11**, 12693 (2021).
8. Myakalwar, A. K. et al. Less is more: Avoiding the LIBS dimensionality curse through judicious feature selection for explosive detection. *Sci. Rep.* **5**, 13169 (2015).
9. Gyftokostas, N., Stefas, D., Kokkinos, V., Bouras, C. & Couris, S. Laser-induced breakdown spectroscopy coupled with machine learning as a tool for olive oil authenticity and geographic discrimination. *Sci. Rep.* **11**, 5360 (2021).
10. Tian, H., Jiao, L. & Dong, D. Rapid determination of trace cadmium in drinking water using laser-induced breakdown spectroscopy coupled with chelating resin enrichment. *Sci. Rep.* **9**, 10443 (2019).
11. Musyoka, W. D., Kalambuka, A. H., Alix, D.-M. & Amiga, K. K. Rapid diagnosis of malaria by chemometric peak-free LIBS of trace biometals in blood. *Sci. Rep.* **12**, 20196 (2022).
12. Killiny, N. et al. Laser-induced breakdown spectroscopy (LIBS) as a novel technique for detecting bacterial infection in insects. *Sci. Rep.* **9**, 2449 (2019).
13. Berlo, K. et al. Laser induced breakdown spectroscopy for the rapid detection of SARS-CoV-2 immune response in plasma. *Sci. Rep.* **12**, 1614 (2022).
14. Khalilian, P. et al. Jewelry rock discrimination as interpretable data using laser-induced breakdown spectroscopy and a convolutional LSTM deep learning algorithm. *Sci. Rep.* **14**, 5169 (2024).
15. Li, C., Feng, C.-L., Oderji, H. Y., Luo, G.-N. & Ding, H.-B. Review of LIBS application in nuclear fusion technology. *Front. Phys.* **11**, 114214 (2016).

16. Maurya, G. S., Marín-Roldán, A., Veis, P., Pathak, A. K. & Sen, P. A review of the LIBS analysis for the plasma-facing components diagnostics. *J. Nucl. Mater.* **541**, 152417 (2020).
17. Van der Meiden, H. J. et al. Monitoring of tritium and impurities in the first wall of fusion devices using a LIBS based diagnostic. *Nucl. Fusion.* **61**, 125001 (2021).
18. Harilal, S. S., Brumfield, B. E., LaHaye, N. L., Hartig, K. C. & Phillips, M. C. Optical spectroscopy of laser-produced plasmas for standoff isotopic analysis. *Appl. Phys. Rev.* **5**, 021301 (2018).
19. Cai, L. et al. Development of an in situ diagnostic system for mapping the deposition distribution on PFC of the HL-2M tokamak. *Rev. Sci. Instrum.* **90**, 053503 (2019).
20. Gonzalez, W. et al. Conceptual studies on spectroscopy and radiation diagnostic systems for plasma control on DEMO. *Fusion Eng. Des.* **146**, 2297 (2019).
21. Almaviva, S. et al. LIBS measurements inside the FTU vessel mock-up by using a robotic arm. *Fusion Eng. Des.* **157**, 111685 (2020).
22. Traparic, I. et al. Resolving studies of Balmer alpha lines relevant to the LIBS analysis of hydrogen isotope retention. *Spectrochim. Acta. Part B* **221**, 107050 (2024).
23. Fantoni, R. et al. Hydrogen isotope detection in metal matrix using double-pulse laser-induced breakdown-spectroscopy. *Spectrochim. Acta. Part B* **129**, 8–13 (2017).
24. Burger, M. et al. Isotopic analysis of deuterated water via single- and double-pulse laser-induced breakdown spectroscopy. *Phys. Plasmas.* **25**, 083115 (2018).
25. LaHaye, N. L., Kurian, J., Diwakar, P. K., Alff, L. & Harilal, S. S. Femtosecond laser ablation-based mass spectrometry: An ideal tool for stoichiometric analysis of thin films. *Sci. Rep.* **5**, 13121 (2015).
26. Sheta, S., Hou, Z., Wang, Y. & Wang, Z. Evaluation of femtosecond laser-induced breakdown spectroscopy system as an offline coal analyzer. *Sci. Rep.* **11**, 15968 (2021).
27. Li, G., Hou, H., Ran, P., Zhao, Y. & Zhong, Z. Calibration-free quantitative analysis of D/H isotopes with a fs-laser filament. *J. Anal. At. Spectrom.* **35**, 1320–1329 (2020).
28. Kautz, E. J., Ronnebro, E. C. E., Devaraj, A., Senor, D. J. & Harilal, S. S. Detection of hydrogen isotopes in zircaloy-4 via femtosecond LIBS. *J. Anal. At. Spectrom.* **36**, 1217–1227 (2021).
29. Kautz, E. J., Devaraj, A., Senor, D. J. & Harilal, S. S. Hydrogen isotopic analysis of nuclear reactor materials using ultrafast laser-induced breakdown spectroscopy. *Opt. Expr.* **29**, 4936 (2021).
30. Mittelmann, S. et al. Hydrogen isotope analysis in W-tiles using fs-LIBS. *Sci. Rep.* **13**, 2285 (2023).
31. Harilal, S. S. et al. Detection of tritium using ultrafast laser-induced breakdown spectroscopy. *J. Anal. At. Spectrom.* **39**, 699–703 (2024).
32. Harilal, S.S. & Kautz, E.J. Analysis of hydrogen and lithium isotopes using Laser-Induced Breakdown Spectroscopy. In *Proc. SPIE* 12939, *High-Power Laser Ablation VIII*, 1293908 (2024).
33. Kurniawan, K. H. et al. Quantitative analysis of deuterium using laser-induced plasma at low pressure of helium. *Anal. Chem.* **78**, 5768–5773 (2006).
34. Kurniawan, K. H., Tjia, M. O. & Kagawa, K. Review of laser-induced plasma, its mechanism, and application to quantitative analysis of hydrogen and deuterium. *Appl. Spectrosc. Rev.* **49**, 323–434 (2014).
35. Pardede, M. et al. High sensitivity hydrogen analysis in zircaloy-4 using helium-assisted excitation laser-induced breakdown spectroscopy. *Sci. Rep.* **11**, 21999 (2021).
36. Ikeda, Y., Soriano, J. K., Ohba, H. & Wakaida, I. Laser ablation plasma expansion using microwaves. *Sci. Rep.* **13**, 13901 (2023).
37. Ikeda, Y., Soriano, J. K., Ohba, H. & Wakaida, I. Analysis of gadolinium oxide using microwave-enhanced fiber-coupled micro-laser-induced breakdown spectroscopy. *Sci. Rep.* **13**, 4828 (2023).
38. Jovicevic, S., Ivkovic, M., Pavlovic, Z. & Konjevic, N. Parametric study of an atmospheric pressure microwave-induced plasma of the mini MIP torch – I. Two-dimensional spatially resolved electron-number density measurements. *Spectrochim. Acta. Part. B.* **55**, 1879–1893 (2000).
39. Jovicevic, S., Ivkovic, M. & Konjevic, N. Parametric study of an atmospheric pressure microwave-induced plasma of the mini MIP torch - II Two-dimensional spatially resolved excitation temperature measurements. *Spectrochim. Acta, Part. B.* **56**(2419), 2428 (2001).
40. Jovicevic, S., Ivkovic, M., Konjevic, N., Popovic, S. & Vuskovic, L. Excessive Balmer line broadening in microwave-induced discharges. *J. Appl. Phys.* **95**(24), 29 (2004).
41. Ciocan, A., Uebbing, J. & Niemax, K. Analytical application of the microwave induced plasma used with laser ablation of solid samples. *Spectrochim. Acta.* **47B**, 611–617 (1992).
42. Matusiewicz, H. Design concept and characterization of a laser ablation - inductively coupled plasma/microwave induced plasma optical emission spectrometric system. *Ecol. Chem. and Eng. S* **16**(S1), 9–17 (2009).
43. Brunnbauer, L. et al. Combined LA-ICP-MS/LIBS: powerful analytical tools for the investigation of polymer alteration after treatment under corrosive conditions. *Sci. Rep.* **10**, 12513 (2020).
44. Yehia-Alexe, S.-A. et al. Considerations on hydrogen isotopes release from thin films by laser induced ablation and laser induced desorption techniques. *Spectrochim. Acta. Part B* **208**, 106774 (2023).
45. Zlobinski, M. et al. Laser-induced desorption of co-deposited deuterium in Beryllium layers on Tungsten. *Nucl. Mater. Energy* **19**(503), 509 (2019).
46. Zlobinski, M. et al. Efficiency of laser-induced desorption of D from Be/D layers and surface modifications due to LID. *Phys. Scr.* **2020**, 014075 (2020).
47. Zlobinski, M. et al. First results of laser-induced desorption - quadrupole mass spectrometry (LID-QMS) at JET. *Nucl. Fusion* **64**, 086031 (2024).
48. NIST Atomic Spectra Database: https://www.nist.gov/pml/atomic-spectra-database (last update to data content: November 2024).
49. Inglis, D. & Teller, E. Ionic depression of series limits. *Astrophys. J.* **90**, 439–448 (1939).
50. Jovicevic, S., Ivkovic, M. & Konjevic, N. Review: Low electron density diagnostics: development of optical emission spectroscopic techniques and some applications to microwave induced plasmas. *Spectrochim. Acta, Part B* **59**, 591–605 (2004).
51. Olivero, J. J. & Longbothum, R. L. Empirical fits to the Voigt line width: A brief review. *J. Quant. Spectrosc. Radiat. Transf.* **17**, 233–236 (1977).
52. Mercadier, L., Hermann, J., Grisolia, C. & Semerok, A. Plume segregation observed in hydrogen and deuterium containing plasmas produced by laser ablation of carbon fiber tiles from a fusion reactor. *Spectrochim. Acta, Part B* **65**, 715–720 (2010).

Acknowledgements

This work was supported by the Ministry of Education, Science and Technological Development of the Republic of Serbia (contract numbers: 451 - 03 - 47/2023 - 01/200024 and 451 - 03 - 47/2023 - 01/200146), the Science Fund of the Republic of Serbia through the NOVA2LIBS4fusion project (grant number: 7753287), within the IDEAS call and under the project: NIFS21 KLPF087. We also acknowledge Stanko Milanović, our technical associate, who drew the schematic figure of the experimental setup.

Author contributions

N. V. – Investigation, Formal Analysis, Visualization, Writing—Review & Editing I. T. – Investigation, Formal Analysis, Writing—Review & Editing B. D. S. – Investigation, Formal Analysis, Writing—Review & Editing D. R. – Investigation, Resources M. K. – Writing—Review & Editing M. I. – Conceptualization, Funding Acquisition, Methodology, Supervision, Writing—Original Draft, Project Administration.

Funding

Ministarstvo Prosvete, Nauke i Tehnološkog Razvoja, 451-03-47/2023-01/200024, 451-03-47/2023-01/200146, Science Fund of the Republic of Serbia, 7753287.

Declarations

Competing interests

The authors declare no competing interests.

Additional information

Supplementary Information The online version contains supplementary material available at https://doi.org/10.1038/s41598-025-96546-x.

Correspondence and requests for materials should be addressed to M.I.

Reprints and permissions information is available at www.nature.com/reprints.

Publisher's note Springer Nature remains neutral with regard to jurisdictional claims in published maps and institutional affiliations.

Eur. Phys. J. Plus (2026) 141:157
https://doi.org/10.1140/epjp/s13360-026-07406-0

THE EUROPEAN PHYSICAL JOURNAL PLUS

Regular Article

Detection of hydrogen isotopes in fusion-relevant targets using laser ablation and microwave-induced plasma

Nikola Vujadinović[1], Ivan Traparić[1], Milivoje Ivković[1,a], Jovan Ciganović[2], Alexandru Anghel[3], Corneliu Porosnicu[3], Ion Mihailescu[3]

[1] Institute of Physics Belgrade - National Institute of the Republic of Serbia, Pregrevica 118, Belgrade 11080, Serbia
[2] Vinca Institute of Nuclear Sciences-National Institute of the Republic of Serbia, University of Belgrade, Mike Petrovića Alasa 12-14, Belgrade 11351, Serbia
[3] National Institute for Laser, Plasma and Radiation Physics, 77125 Magurele, Bucharest, Romania

Received: 2 August 2025 / Accepted: 3 February 2026

Abstract The analysis of plasma facing components (PFCs) of fusion machines using LIBS (Laser-induced breakdown spectroscopy) technique is widely spread throughout fusion community. Difficulties arise when spectroscopic measurements of tritium retention are performed. Particularly, resolving the deuterium (D_α) and tritium (T_α) Balmer alpha lines becomes a major issue. Therefore, this study exploits the usage of microwave-induced plasma (MIP) as a potential solution for the aforementioned difficulties. The target material was introduced into MIP via Nd:YAG laser ($\lambda = 1.064$ μm) ablation, while the spectral signals were monitored with a high-resolution spectrometer and ICCD camera. Two silicon-based targets were used in experiments. The first Si target, coated with carbon (C) and exposed to methane (CH_4), was used for optimization of the measurement system. The second one, coated with C and implanted with deuterium (D), was used for the final measurements. The final measurements suggest that, with the current setup, the lowest detectable tritium level corresponds to a T_α line intensity of 35–50% of the D_α line intensity. This stands, in our opinion, for a promising method, allowing a reliable and fast determination of tritium content retained in the material.

1 Introduction

Generation of enough, non-polluting energy resources stands among major provocations for today's modern society. Nuclear fusion is a promising alternative to replace modern coal and gas fired power plants as it is a clean, reliable, and green energy source which does not leave behind long-lasting radioactive waste. The long journey toward stable reactor and results achieved so far inspired the construction of tokamak ITER, a project sustained by an world-wide international consortium [1].

Maintenance and diagnostics of plasma facing components (PFCs) represent at this moment a key task in order to ensure the stable operation of future fusion reactors. During operation, PFCs are exposed to various stresses, heat loads, neutron fluxes, etc. Among other processes, monitoring the composition of PFCs material and amount of retained fuel in them due to plasma exposure is important [2–6]. Fuel retention must be monitored because of its impact on fuel efficiency, plasma density, and density of neutral hydrogen at plasma boundary [2]. Additionally, due to tritium radioactivity, any in situ tritium retention study would need to be conducted remotely using a robotic arm capable of reaching all positions inside the vessel [7, 8].

Different methods have been applied for analysis of isotope retention. In particular, ion beam analysis (IBA), which can be realized in setups like nuclear reaction analysis (NRA) or elastic recoil detection analysis (ERDA), is well developed methods for ex situ investigation of hydrogen isotope retention [3, 9–11]. One should also mention, in this context, the thermal desorption spectroscopy (TDS) combined with mass spectroscopy to detect hydrogen isotopes [12].

Several authors extended laser-induced breakdown spectroscopy (LIBS) technique to analyze the content of PFC materials, as documented in dedicated review articles [13–15]. LIBS was also extensively studied as a potential tool for hydrogen isotope analysis. The main difficulty for this type of LIBS application is Stark broadening of hydrogen lines, which limits the resolution of the method, especially the resolving of tritium (T_α) and deuterium (D_α) Balmer alpha lines. Isotope lines, D_α and H_α, were identified but only partially resolved on EAST tokamak, where a custom made in situ LIBS setup was used [16]. Alamri et al. [17] studied microwave-enhanced LIBS where they have managed to lower the Stark broadening and resolve D_α and H_α lines, but not fully, which is necessary if one wishes to resolve the Balmer alpha lines of tritium and deuterium. Fantoni et al. [18] studied the application of double pulse LIBS setup in vacuum for detection of hydrogen isotopes with two Nd:YAG lasers, both working at fundamental harmonic (1064 nm) and energy of 170 mJ. The obtained D_α and H_α spectral lines were resolved according to the

[a] e-mail: ivke@ipb.ac.rs (corresponding author)

Published online: 13 February 2026

Rayleigh criterion. A superior resolution, i.e., FWHM of H_α line of 0.05 nm at a helium pressure of 10 Torr and camera delay of 26 μs, was reported by Kautz et al. [19, 20], where they irradiated Zircaloy-4 targets with fs pulses generated by a Ti:sapphire laser source. Kautz et al. [21] used an orthogonal double pulse scheme in helium atmosphere, illuminated by two Nd:YAG lasers sources ($\lambda = 1.064$ μm) to resolve D_α and H_α lines. They observed that D_α line intensity and FWHM increased 30 and 2 times, respectively, with the increase of He pressure. Traparić et al. [22] studied the resolving of D_α and T_α lines based on single pulse LIBS setup with transversely excited atmospheric (TEA) CO_2 laser on graphite-based targets. The increase of D_α line intensity with increase in He pressure was also observed, as in [21], while the optimal conditions for full separation of D_α and H_α were obtained in He atmosphere at 40 mbar of pressure and camera delay of 20 μs, where the stated FWHM of D_α line was 0.038 nm. In [22], the authors also suggested the plasma conditions necessary for resolving of T_α and D_α lines for available spectrometer.

The unique attempt to date for extending LIBS to direct tritium detection was by Harilal et al. [23], where they used fs laser ablation to investigate the depth profiling of retained tritium in neutron irradiated Zircaloy-4. However, although H_α and T_α peaks have been resolved, the widths of the two lines are still too broad for simultaneous detection of all three isotopes.

One should also mention that laser ablation (LA) and laser-induced desorption (LID), were used for material introduction into different types of measuring devices. Thus, Schweer et al. [24] used LID with a free running ruby laser source coupled to a quadrupole mass analyzer to monitor the deuterium content in test limiter of TEXTOR and in divertor of JET tokamak in laboratory (after the samples were demounted from reactor). ITER-graded tungsten samples coated with thin layers of beryllium (Be) and D were used for LID investigation by Zlobinski et al. [25] to assess the quantity of retained D atoms in the Be layer via mass spectrometry at FREDIS setup [26]. Recently, Zlobinski et al. [27] performed an in situ analysis of retained fuel at JET, where LID was performed with a diode pumped ytterbium fiber laser, while detection was conducted with a mass spectrometer. The release of hydrogen isotopes from thin films and Be coatings using LA and LID was also studied by Yehia-Alexe et al. [28, 29], where the investigation was conducted by optical emission and mass spectroscopy, respectively.

However, much less work has been done in coupling LA or LID with appropriate plasma sources as a simple and cost-effective solution for ex or in situ analysis. For example, microwave-induced plasma (MIP) operating at atmospheric pressure [30, 31] has plasma parameters suitable for resolving D_α and T_α lines. Moreover, MIP operating at low pressures can have even smaller electron densities, which further minimizes the Stark and van der Waals broadening effects, resulting in a dominant Doppler and instrumental broadening effects. This was demonstrated in the work of Vujadinović et al. [32], where it was shown that LID can serve as a suitable D introduction method into MIP. The full separation of H_α and D_α was achieved, while the FWHM of D_α line was measured to be 0.033 nm, which provides excellent experimental conditions for accurate resolving of D_α and T_α lines.

In this work, we investigated whether an improvement for spectral resolving of T_α and D_α lines can be achieved through coupling of LA and MIP. To this aim, LA process was studied and an appropriate experimental setup was proposed to test the depth profiling potential using targets consisting of layers of C + D and C + CH_4 on Si substrate.

2 Experiment

The setup used in experiments to study hydrogen isotope retention is depicted schematically in Fig. 1. A low-pressure MIP, ignited inside the capillary tube having an outer/inner diameters of 8/2 mm, was used as the plasma source for excitation and analysis of characteristic hydrogen isotope Balmer alpha lines. The capillary is attached to the specially made ablation chamber, equipped with a target rotator mechanism and an entrance window ensuring the laser radiation incidence onto target at ~ 45 degrees. The residual pressure inside capillary was pumped down to ~ 0.5 mbar, prior to argon filling. The capillary was placed inside a Beenakker resonator, connected to a microwave power supply (AHF Analyses Technik GMW 24-301 DR 2.45 GHz), generating a power of maximum 100 W. The material was introduced into MIP via laser ablation with a Quantel 450 Nd:YAG laser source generating pulses of 1.064 μm wavelength, 450 mJ maximum energy, and 6 ns pulse duration at a frequency repetition rate of 10 Hz. The laser beam was focused with an AR-coated lens of 12.5 cm focal length onto the target surface.

The light emitted by MIP was collected through an optical window placed at the end of the capillary using a collimator (COLL) and guided via an optic fiber to a high-resolution spectrometer (SOL instruments MS7504i spectrometer equipped with a grating 1800 g/mm). The spectrometer is equipped with an Andor iStar DH734-18F-63 ICCD camera (1024 × 1024 pixels of 13 μm pixel size). An external digital delay generator (Stanford Research SRS 535) triggered by the signal commanding the opening of the Nd:YAG laser Q switch was used for the delay control and camera gating. The separation of the emission processes created by LIBS and MIP can be achieved by changing the delay time of camera exposure, as LIBS signals are typically on the microsecond-time scale, while the transport of the ablated material to the MIP takes place over a millisecond-time scale.

Morphological investigation of sample surface was carried out with a non-contact optical profilometer Zygo NewView 7100 (Zygo, Middlefield, Connecticut, USA), equipped with a 5 × magnifying objective and operated in a downward scanning regime. It covers a vertical scan range of 150 μm with a resolution < 0.1 nm, whit possibilities for extension up to 20 mm.

Two silicon-based targets were used in experiments. The first one was coated with a 1-μm-thick hydrogenated carbon layer by 80 W Radio Frequency Magnetron Sputtering (RF MS) from a pure carbon target in a 3×10^{-2} mbar mixture of argon (Ar) and methane (CH4), flowing with a rate of 20 and 35 sccm, respectively. The second target was coated with a 100 nm layer of C and D

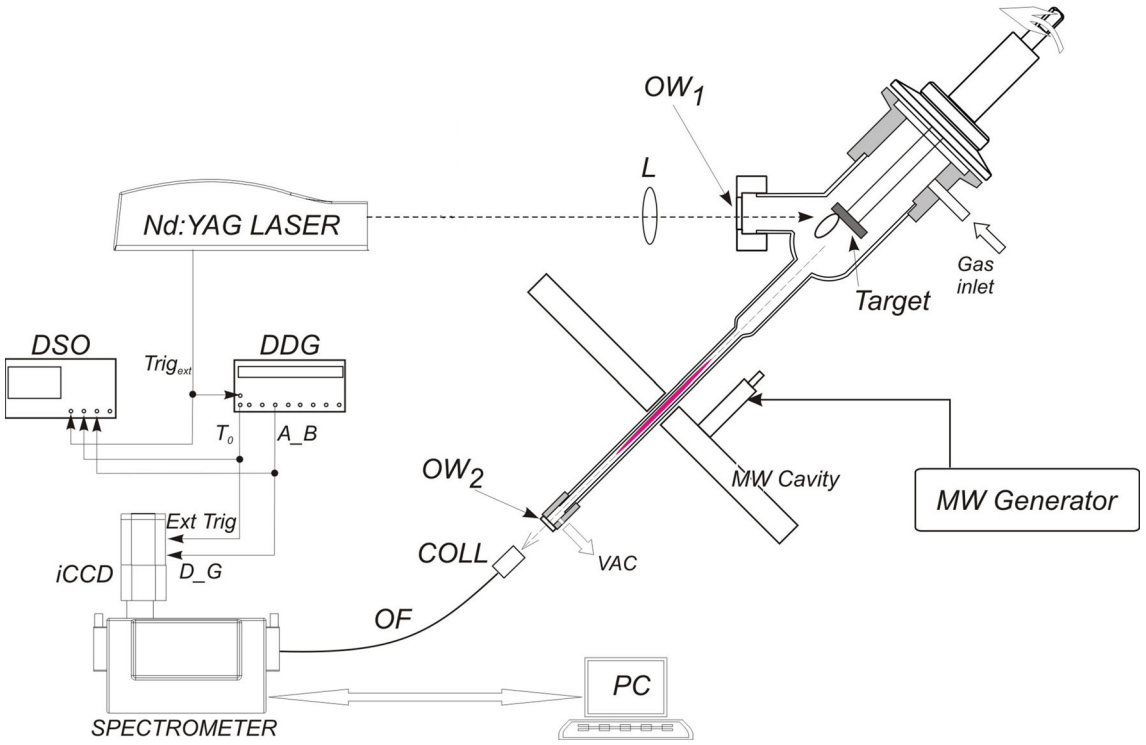

Fig. 1 Experimental setup for Nd:YAG laser ablation used to generate species for introduction into a microwave-induced plasma (MIP): DSO (digital storage oscilloscope), DDG (digital delay generator), COLL (collimator of the emitted radiation into fiber), OF (optical fiber), VAC (vacuuming port), L (focusing lens), and OW (optical windows)

by 190 W Direct Current Magnetron Sputtering (DC MS) in a 1×10^{-2} mbar mixture of Ar and D, flowing with a rate of 5 and 48 sccm, respectively.

3 Results and discussion

First, the optimal camera delay time for a fixed gate time was determined, followed by investigation of the ablation rate. It was important to obtain the lowest ablation rate possible that is still providing the detection with a satisfactory signal/noise ratio. After that, the optimal MIP power was determined with respect to H_α line intensity and FWHM.

The plasma temperature was inferred from Boltzmann plot of the Ar I lines, while the electron density was estimated from H_α line by fitting the convolved theoretical Stark broadening profile with instrumental and Doppler widths. The theoretical detection limit for tritium content in the target was finally estimated on these bases for the given plasma parameters.

Before starting the Ar flow, the chamber was evacuated to the pressure of 0.5 mbar. In [32], it was found that the optimal Ar pressure for the ablated material transport is between 15 and 20 mbar, so, in this work, the pressure was fixed to 15 mbar for a more stable MIP operation, but influences of camera delay time and MIP power needed to be investigated again because of the shorter capillary in the current setup.

3.1 Delay time

We next investigated the time interval when the ablated material from the C + CH_4 target was present in the MIP discharge by properly adjusting camera delay time. Working pressure affects when the material will be present in the MIP discharge area, and that determines when the spectral lines are emitted and can be detected. By varying the camera delay time, time interval when the ablated material is present in the MIP discharge can be estimated.

One mentions here that the C I and C II lines have been observed in [33, 34] by studying laser-generated plasmas on carbon-based targets, but for superior laser fluences (900 J/cm^2 in [34]) than reported in this work. However, in a microwave-induced plasma (MIP) with low electron temperatures, C II emission is unlikely, and no C I lines were detected in our setup either. One possible explanation could be that the most prominent C I line (247.86 nm) might have been emitted, in our case as well, but was not detected due to the limited transmission of optical window OW2 (BK7 glass) used in our setup. Under these constraints, the observation is possible of C-based molecular bands only, which are expected to be present in MIP, for these rather low electron temperatures.

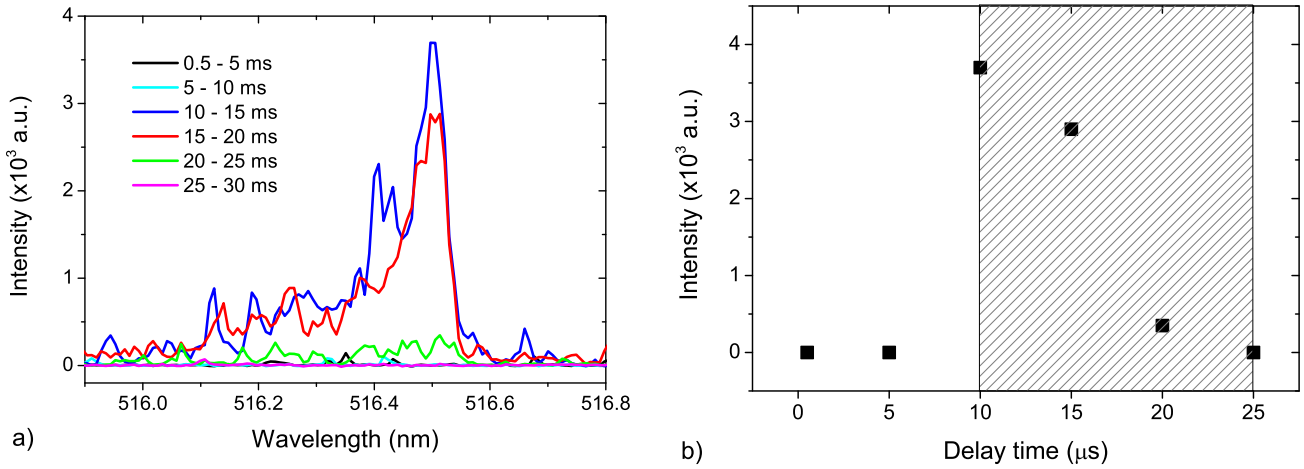

Fig. 2 **a** The (0–0) band spectra of the Swan system and **b** dependence of the intensity of the band head at 516.5 nm on camera delay time for a fixed gate time of 5 ms (experimental conditions: $p_{Ar} = 15$ mbar; $E_{laser} = 97$ mJ; $P_{MIP} = 40$ W; target: C + CH_4)

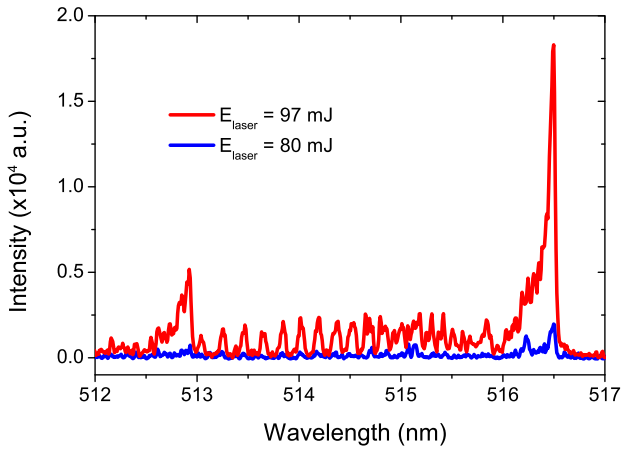

Fig. 3 Effect of decreasing the laser energy on the ablation rate (experimental conditions: $p_{Ar} = 15$ mbar; $P_{MIP} = 40$ W; recording window: 10–25 ms; target: C + CH_4)

The C_2 molecule's Swan system (0–0) band (d3Πg → a3Πu) was therefore selected for recording, a relatively intense spectrum, characterized by a dissociation energy of 6.2 eV, and a rather low excitation energy of 2.4 eV [22].

The (0–0) band spectra of the Swan system are shown in Fig. 2a, while the dependence of the intensity of the band head at 516.5 nm versus camera delay time is given in Fig. 2b. To avoid possible interferences with LIBS spectra, the delay time for the first measurement was set to 0.5 ms, so the gate time was 4.5 ms. For all other measurements, the gate time was 5 ms.

As can be seen from Fig. 2b, the time it takes for material to reach MIP discharge area is about 10 ms, and is present until 25 ms, so the optimal time window for spectroscopic measurements is with the camera delay of 10 ms and gate time of 15 ms (shaded area in Fig. 2b).

3.2 Ablation rate

The proxy target C + CH_4 on Si substrate was next used to estimate the optimal ablation rate. The working regime assumes, as with the previous section, the use of minimal ablation rate while maintaining good signal to noise ratio. It is generally accepted [35] that the IR laser radiation absorption in generated plasma plumes mainly proceeds by inverse bremsstrahlung (IB) which follows a λ^3 dependence. Consequently, the use of the fundamental harmonic ($\lambda = 1.064$ μm) of the Nd:YAG laser source in our experiments strongly favors IB and therefore reduces the ablated mass.

The (0–0) C_2 Swan band was monitored for the investigation of the optimal laser energy transfer. As can be seen in Fig. 3, the signal-to-noise ratio for the laser energy of 97 mJ is good, but when the energy decreases to 80 mJ, the intensity of the band decreases significantly and the signal-to-noise ratio gets worse.

Figure 3 shows that with a decrease in the ablation rate, the intensity of the C_2 band drops sharply. This may relate to the transport efficiency of the ablated mass, as less mass is coming to MIP. So, for the optimal laser, energy 97 mJ was selected for further investigations.

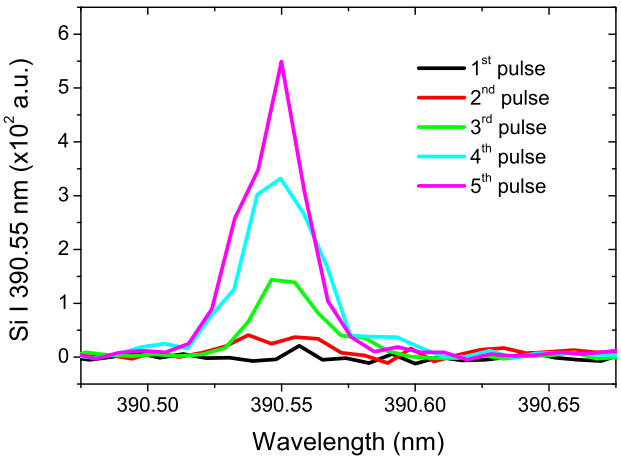

Fig. 4 Spot profile of five successive laser shots at the same place and the intensity of Si I 390.55 nm line for every laser shot taken (experimental conditions: $p_{Ar} = 15$ mbar; $E_{laser} = 97$ mJ; $w_{slit} = 50$ μm; recording window: 1–11 μs; target: C + CH_4)

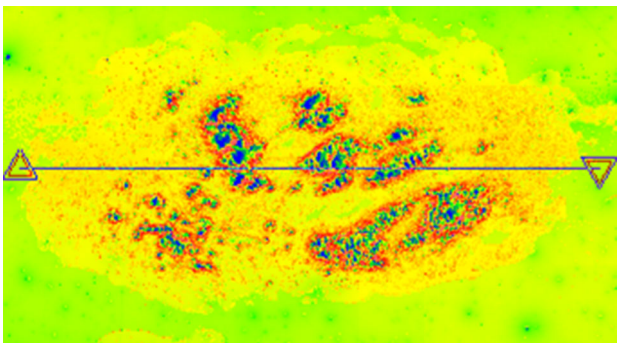

Fig. 5 Spot profile on the C + CH_4 target after five consecutive laser shots recorded with profilometer

LIBS signal was monitored to further study the ablation rate by choosing the delay and gate time of 1 and 10 μs, respectively. The spectrometer slit width was set to $w_{slit} = 50$ μm in order to capture a stronger signal. Five laser shots were fired onto the same place, and profilometry measurements were performed on this spot. Signal from Si I 390.55 nm line ($3s^2 3p4s \rightarrow 3s^2 3p^2$) is given in Fig. 4, while the corresponding spot profile is shown in Fig. 5. It should be noted that the spot profile has an elliptical shape because the laser beam (circular shape) hits the target at an acute angle (see Fig. 1). Based on the shot-by-shot line intensities from Fig. 4, we determine the ablation rate of ~ 400 nm /shot, as Si I line appears after the third shot at the same spot on the target.

From profilometry measurements, it was concluded that the size of the spot on the target is an ellipse with the largest diameter of 2.1 mm, and the smallest diameter of 1.1 mm, thus having a surface of 0.018 cm^2. Therefore, with an optimal laser energy of 97 mJ and a spot size of 0.018 cm^2, we determine that the optimal laser fluence is 5.4 J/cm^2.

Profilometry measurements suggest a non-uniform ablation of the target, characterized by the presence of local "hotspots". It is assumed that most of the material comes from these spots. Better control of the ablation process is expected with picosecond or femtosecond lasers [36].

3.3 Optimal MIP power

The influence of power supplied to the microwave cavity was studied from the perspective of FWHM and intensity of hydrogen Balmer alpha line from the MIP, without laser ablation. Hydrogen atoms were present in the MIP, probably as a residual gas on the chamber walls, or as moist. The slit of the spectrometer was now set to 20 μm in order to obtain narrower spectral lines. The dependence of FWHM on MIP power is shown in Fig. 6a while the influence of power supplied on the intensity of H_α line is shown in Fig. 6b.

As can be seen in Fig. 6a, the FWHM of H_α line fluctuates very little around 0.045 nm with the change of MIP power. Similar measured hydrogen FWHMs were reported by Jovićević et al. [37] in the similar experimental setup using MIP source at low pressure, where authors reported Balmer line broadening with admixtures of Ar and He with 3% of hydrogen.

The intensity of the H_α increases with the increase in power supplied by the generator (Fig. 6b), as the plasma column within the capillary extends further along the discharge tube, increasing the plasma volume. When the power reaches around 50–60 W, the plasma approaches the section with the optical window and vacuum hose. Therefore, for the purpose of safety of experimental apparatus, a power value of 40 W was chosen, at which the reflected power was measured to be 3 W.

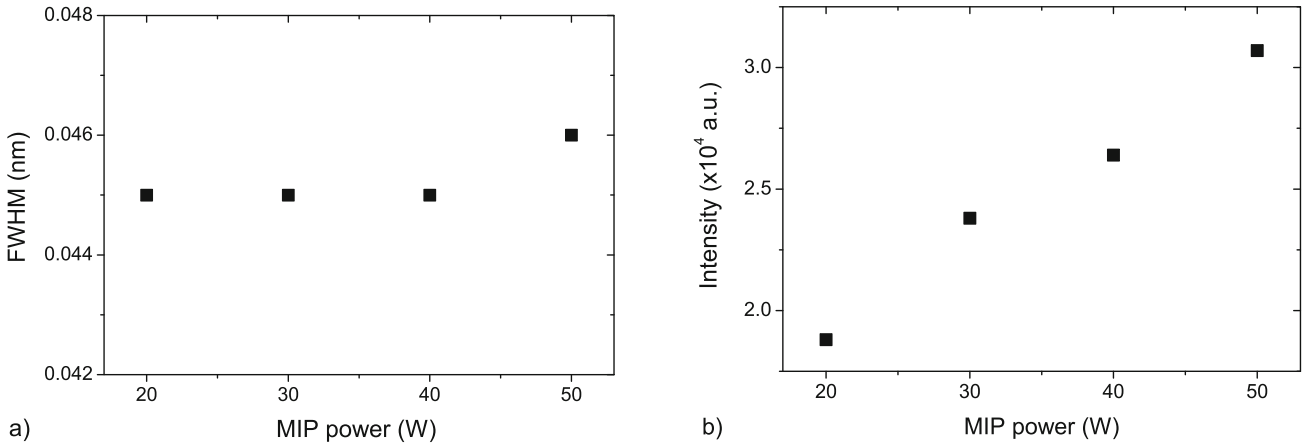

Fig. 6 Dependence of **a** FWHM and **b** intensity of H_α line on the power supplied to the microwave cavity (experimental conditions: $p_{Ar} = 15$ mbar; $w_{slit} = 20$ μm; target: C + CH_4)

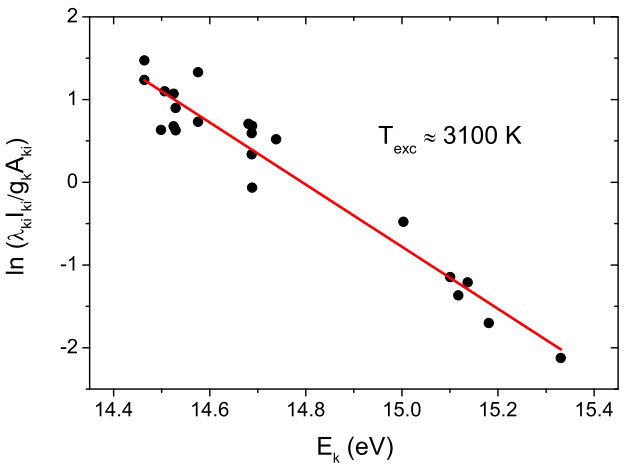

Fig. 7 Boltzmann plot of the Ar I lines for excitation temperature estimation

3.4 Plasma diagnostics

The excitation temperature was estimated from the Boltzmann plot of Ar I lines to be 3100 K. Boltzmann plot is given in Fig. 7, and the complete data for the lines used to obtain the Boltzmann plot can be found in Table S1 of the supplementary material.

The estimation of electron density was obtained through the comparison of generated H_α line profile using the CS tables [38]. For computation of the profiles, the gas temperature was set to be 3100 K, which was obtained from the Boltzmann plot, and instrumental width for the spectrometer slit width of 20 μm was measured with Oriel Penlight Hg spectral lamp to be 0.025 nm. Relative mass, that includes the effect of movement of ions, was set to $\mu = 1$ for mixture of hydrogen, deuterium, and argon plasma constituents. Generated profiles, together with experimentally recorded H_α line, are shown in Fig. 8.

From Fig. 8, it is estimated that the most probable plasma electron density is around 2.1×10^{20} m^{-3} as it fits the experimental measurements the best. For the same FWHM, but with deconvolution of the Balmer alpha spectral line, Jovićević et al. [37] found that the electron density is around 7×10^{19} m^{-3}. As the deconvolution formulas are not tested well below the electron density values of 10^{20} m^{-3}, authors believe that the estimation in this paper is more accurate.

3.5 Detection of D_α from carbon target

With the optimized camera delay time, ablation rate, and MIP power, the measurements of detection and resolution of H_α and D_α were performed using the C + D target. The measurement with three consecutive laser shots at the same spot is given in Fig. 9.

As the ablation is high at the hotspots, the D_α signal is the strongest after the first shot. Since the thickness of deposited D is 100 nm and at the ablation at the hotspots was estimated to be 400 nm, the D_α signal decreases substantially with every consecutive shot.

To improve signal to noise ratio, five accumulations were performed under the same conditions, where each time laser was fired onto the fresh spot on the target. The result of the accumulations is shown in Fig. 10a. FWHMs of the lines were estimated from

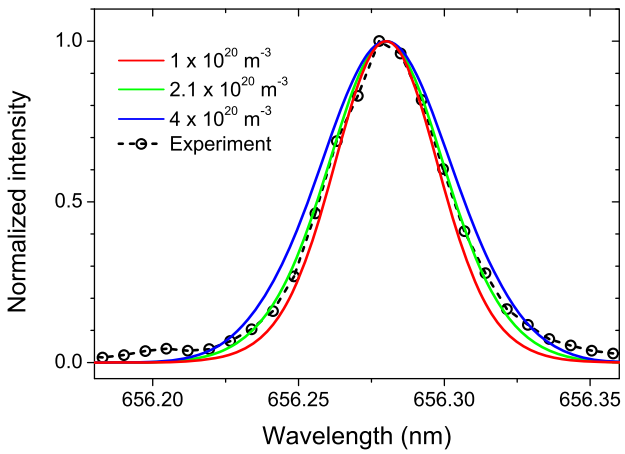

Fig. 8 Generated profiles of H_α together with the experimentally measured profile (FWHM of 0.047 nm) from MIP plasma without laser ablation (parameters for computation: $T_e = T_g = 3100$ K; $\mu = 1$; $w_i = 0.025$ nm)

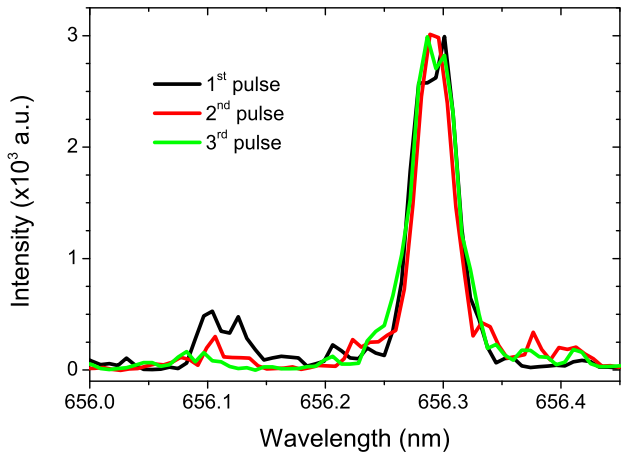

Fig. 9 Detection of D_α from carbon target (experimental conditions: $p_{Ar} = 15$ mbar; $P_{MIP} = 40$ W; $E_{laser} = 97$ mJ; $w_{slit} = 20$ μm; recording window: 10–25 ms; single pulses at the same spot)

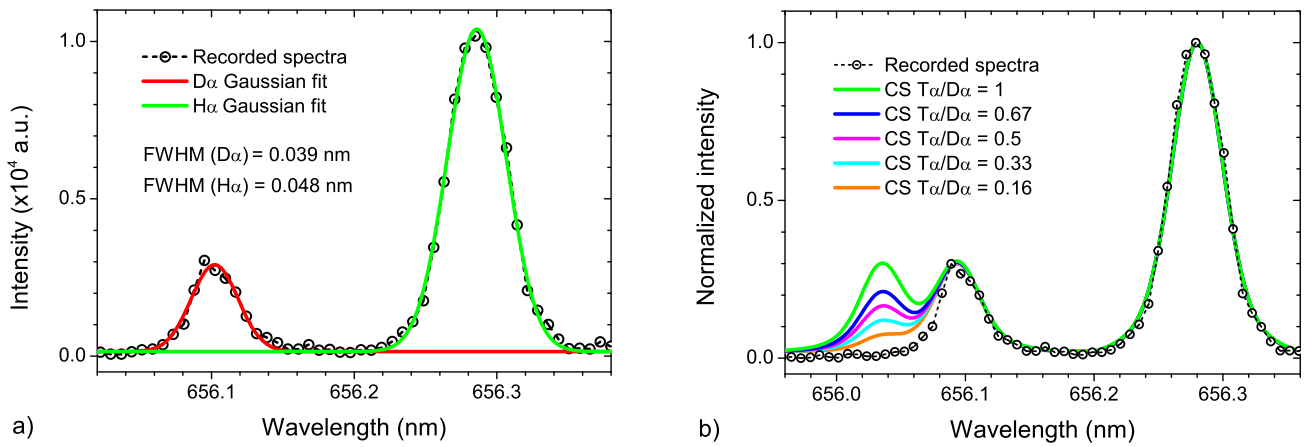

Fig. 10 **a** Experimental estimation of FWHM of H_α and D_α lines (experimental conditions: $p_{Ar} = 15$ mbar; $P_{MIP} = 40$ W; $E_{laser} = 97$ mJ; $w_{slit} = 20$ μm; recording window: 10–25 ms; five accumulations) and **b** theoretical estimation of tritium resolving for current experimental conditions (parameters: $N_e = 2.1 \times 10^{14}$ cm^{-3}, $T_g = 3100$ K, $T_e = 3100$ K, $w_i = 0.025$ nm and $\mu = 1$)

fitting the lines with a Gauss function, but also with human measurement to ensure that the fit values were correct. The estimated line width from the fit is 0.048 nm for H_α and 0.039 nm for D_α.

The study by Traparić et al. [22] emphasized that fulfilling necessary conditions for resolving D_α and T_α required full resolution of H_α and D_α lines, while ensuring the dip between these lines was less than 10% of the smaller peak intensity. As can be seen in

Table 1 Valley-to-peak ratios for different T_α-to-D_α intensity ratios, based on the CS-generated profiles shown in Fig. 10b

$\frac{I_{T_\alpha}}{I_{D_\alpha}}$	R_{vp}
1	0.57
0.67	0.67
0.5	0.76
0.33	0.88
0.16	No valley

Fig. 10a, this condition is more than satisfied, as the dip is less than 4% of the D_α intensity. By using the formula for the critical FWHM of D_α at which D_α and T_α would be resolved [22],

$$FWHM_{cr}(D_\alpha) = 0.0599 - 0.0388 \bullet e^{-1.765\frac{I_{T_\alpha}}{I_{D_\alpha}}} \tag{1}$$

and setting $FWHM_{cr}$ (D_α) to the experimentally obtained value of 0.039 nm, the critical intensity ratio of T_α and D_α for which lines would still be resolved was calculated to be $R_{cr} = (I_{T\alpha}/I_{D\alpha})_{cr} = 0.35$.

The estimation of the resolution power for separating the D_α and T_α lines was also calculated for H_α, D_α, and T_α profiles (Fig. 10b), generated with CS tables in the following way: Stark profiles for H_α, D_α, and T_α were generated using the CS tables with the assumption of same Stark width for all three lines. This approximation was discussed in [22] where it was concluded that it is a valid approximation to make. Then, the profiles were convolved with the corresponding Doppler and instrumental profile, where temperature used to get Doppler width was one obtained from Boltzmann plot. The corresponding profiles were normalized to the intensity of H_α line, and intensity of T_α was varied between 16% of intensity of D_α and the hypothetical case where both lines would have the same intensity. FWHMs obtained with CS theory are $w_{H\alpha} = 0.047$ nm, $w_{D\alpha} = 0.042$ nm, and $w_{T\alpha} = 0.041$ nm for the assumed electron density of 2.1×10^{20} m^{-3}.

The estimation of the resolution power for separating the D_α and T_α lines is expressed using the factors R_c and R_{vp}. Factor R_c defined as

$$R_c = \frac{2\Delta\lambda}{w_1 + w_2} \tag{2}$$

is commonly used in chromatography to evaluate the resolution of two nearby peaks. This criterion was also used by Almaviva et al. [39] to evaluate the resolution criterion for D_α–T_α and D_α–H_α for LIBS plasma at atmospheric pressure in different gas environments. The peaks are considered resolved if the condition $R_c \geq 1$ is satisfied. Here, $\Delta\lambda$ represents the separation of the peaks, while w_1 and w_2 are the FWHMs of the lines. Chromatographic resolution assumes Gaussian-profile peaks of equal intensity, so Eq. 2 was used to calculate the R_c factor in a hypothetical case where both lines have the same intensity. For a peak separation $\Delta\lambda = 0.055$ nm and widths $w_{D\alpha} = 0.042$ nm and $w_{T\alpha} = 0.041$ nm, we obtain $R_c = 1.33$, which satisfies the chromatographic criterion for resolving two nearby peaks. In [39], the authors best reported values were 1.52 for D_α–H_α and 0.44 for D_α–T_α. The result reported in our work may even be a slight underestimation of the actual resolution, as the FWHM of the generated D$_\alpha$ profile (0.042 nm) is larger than the experimentally measured profile (0.039 nm).

Factor R_{vp} represents the valley-to-peak ratio and is defined as

$$R_{vp} = \frac{I_{valley}}{\min(I_1, I_2)} \tag{3}$$

where I_{valley} is intensity at the minimum point between two peaks and the $\min(I_1, I_2)$ is the intensity of the smaller of the two peaks. Here, a lower value indicates better resolution, and the criterion for resolving is formulated as $R_{vp} \leq 0.8$. Valley-to-peak ratio is especially useful when nearby peaks are not of equal intensity. The R_{vp} factors corresponding to the profiles from Fig. 10b are given in Table 1. Based on this criterion, the proposed setup can resolve T_α and D_α lines when the ratio of their intensities is a little less than 50%.

4 Conclusion

In this work, the possibility of coupling the laser ablation process together with MIP to detect hydrogen isotopes was investigated. The targets that were used in this study were C + CH_4 target as a proxy for optimization purposes and C + D target for measurement purposes.

Profilometry measurements together with spectroscopic measurements indicate that the optimal laser fluence, based on the minimal ablation rate that led to a measurable signal and good signal-to-noise ratio in MIP plasma, is around 5.4 J/cm^2. Analysis of Si *I* line intensities indicates that the ablation rate was around 400 nm, but profilometry yielded results that indicate that the ablation

from the surface of the material was not homogeneous, therefore disabling the precise and controlled depth profile measurements. Further enhancements can be achieved if a picosecond or femtosecond laser (instead of a nanosecond) is employed for laser ablation.

High resolution spectroscopic measurements demonstrated that this setup enables monitoring and detection of tritium in the fusion-relevant samples. Namely, H_α and D_α lines are completely resolved, with the intensity of the dip between them being less than 4% of the weaker line (D_α). The critical intensity ratio of T_α and D_α for which lines would still be resolved [22], based on the experimentally obtained D_α FWHM, was calculated to be $R_{cr} = 0.35$. Tritium and deuterium resolving estimations were also calculated for line profiles generated with CS tables. For T_α and D_α peaks of same intensities, chromatographic resolution power was calculated to be $R_c = 1.33$, which satisfies the chromatographic criterion for resolving two nearby peaks. For different T_α and D_α peak intensities, valley-to-peak ratio was used to estimate that the proposed setup could resolve T_α and D_α lines when the ratio of their intensities is a little less than 50%. These results can be further improved if a spectroscopic system with an even higher resolution is used.

It should be noted that our proposed method can be applied to monitor hydrogen isotope retention using a specially designed measuring head for plasma fusion reactor wall diagnostics. A functional model of this head is presented in the work of Ivković et al., currently under peer review. For deuterium retention studies in fusion-relevant plasma reactors that do not contain tritium, a manually operated telescopic arm equipped with the measuring head can be used. For tritium retention studies, however, the measuring head should be mounted on a robotic arm and operated remotely.

It should also be emphasized that the described method is more optimal for resolving deuterium and tritium alpha lines than many other LIBS setups, including microwave-enhanced LIBS, due to smaller Stark broadening of hydrogen lines in MIP.

Beyond hydrogen isotope retention studies, the proposed method can also be applied for improving accuracy of various analytical techniques that suffer from poor spectral resolution. In addition, it is much simpler than methods based on laser ablation followed by inductively coupled plasma mass spectrometry (LA-ICP-MS). While it typically has lower detection sensitivity than LA-ICP-MS, our method offers an advantage in terms of portability and in situ applications.

Supplementary Information The online version contains supplementary material available at https://doi.org/10.1140/epjp/s13360-026-07406-0.

Acknowledgements We acknowledge S. Anghel for assistance with language corrections.

Author contributions Conceptualization was contributed by Milivoje Ivković and Corneliu Porosnicu; Methodology was conducted by Milivoje Ivković; Formal analysis and investigation were performed by Nikola Vujadinović, Ivan Traparić, and Jovan Ciganović; Writing–original draft preparation was done by Nikola Vujadinović, Ivan Traparić, and Alexandru Anghel; Writing–review and editing was done by Nikola Vujadinović, Ivan Traparić, and Milivoje Ivković; Software was carried out by Ivan Traparić; Visualization was performed by Nikola Vujadinović; Funding acquisition was performed by Milivoje Ivković and Corneliu Porosnicu; Resources were provided by Alexandru Anghel and Corneliu Porosnicu; Project administration was carried out by Milivoje Ivković and Corneliu Porosnicu; Validation was carried out by Corneliu Porosnicu and Ion Mihailescu; Supervision was carried out by Milivoje Ivković, Corneliu Porosnicu, and Ion Mihailescu.

Funding This work was funded by Ministry of Science, Technological Development, and Innovations of the Republic of Serbia under the contract numbers: 451-03-66/2024-03/200024 and 451-03-47/2023-01/200017 and supported by the Science Fund of the Republic Serbia, Grant no. 7753287 "NOVA2LIBS4fusion". INM acknowledges with thanks that this research was partially funded by a grant from the Ministry of Education and Research, CCCDI—UEFISCDI, project number 90058/16.09.2025, within PNCDI IV. We also acknowledge funding from IFA on project ELI-RO-19 "HighprotonPlas".

Data availability The data that support the findings of this study are available from the corresponding author upon reasonable request.

Declarations

Conflict of interest The authors declare no competing interests.

References

1. Fusion Energy and ITER. (2024), https://research-and-innovation.ec.europa.eu/research-area/energy/fusion-energy_en.
2. L. Qiao, X. Zhang, R. He, H. Zhang, E. Fu, P. Wang, Spectrochim. Acta B At. Spectrosc. **173**, 105975 (2020)
3. C. Cupak, E. Pitthan, M.V. Moro, M. Fellinger, D. Primetzhofer, F. Aumayr, Nucl. Mater. Energy **33**, 101249 (2022)
4. M. Yajima, S. Masuzaki, N. Yoshida, M. Tokitani, T. Otsuka, Y. Oya, Y. Torikai, G. Motojima, LHD Experiment Group, Nucl. Mater. Energy **27**, 100906 (2021)
5. J. Roth, E. Tsitrone, T. Loarer, V. Philipps, S. Brezinsek, A. Loarte, G.F. Counsell, R.P. Doerner, K. Schmid, O.V. Ogorodnikova, Plasma Phys. Control. Fusion **50**, 103001 (2008)
6. A. Zakharov, A. Gorodetsky, V.K. Alimov, S. Kanashenko, A. Markin, J. Nucl. Mater. **241**, 52 (1997)
7. R. Skilton, N. Hamilton, R. Howell, C. Lamb, J. Rodriguez, Fusion Eng. Des. **136**, 575 (2018)
8. S. Almaviva, L. Caneve, F. Colao, V. Lazic, G. Maddaluno, P. Mosetti, A. Palucci, A. Reale, P. Gasior, W. Gromelski, Fusion Eng. Des. **157**, 111685 (2020)
9. M. Mayer, S. Möller, M. Rubel, A. Widdowson, S. Charisopoulos, T. Ahlgren, E. Alves, G. Apostolopoulos, N.P. Barradas, S. Donnelly, Nucl. Fusion **60**, 025001 (2019)
10. Y. Oya, H. Fujita, C. Hu, Y. Uemura, S. Sakurada, K. Yuyama, X. Li, Y. Hatano, N. Yoshida, H. Watanabe, Nucl. Mater. Energy **9**, 84 (2016)
11. V.K. Alimov, M. Yajima, S. Masuzaki, M. Tokitani, LHD Experiment Group, Fusion Eng. Des. **147**, 111228 (2019)

12. Y. Oya, C. Hu, H. Fujita, K. Yuyama, S. Sakurada, Y. Uemura, S. Masuzaki, M. Tokitani, M. Yajima, Y. Hatano, Fusion Sci. Technol. **71**, 351 (2017)
13. C. Li, C.-L. Feng, H.Y. Oderji, G.-N. Luo, H.-B. Ding, Front. Phys. **11**, 1 (2016)
14. G.S. Maurya, A. Marín-Roldán, P. Veis, A.K. Pathak, P. Sen, J. Nucl. Mater. **541**, 152417 (2020)
15. H. Van Der Meiden, S. Almaviva, J. Butikova, V. Dwivedi, P. Gasior, W. Gromelski, A. Hakola, X. Jiang, I. Jõgi, J. Karhunen, Nucl. Fusion **61**, 125001 (2021)
16. D. Zhao, C. Li, Z. Hu, C. Feng, Q. Xiao, R. Hai, P. Liu, L. Sun, D. Wu, and C. Fu, Rev. Sci. Instrum. **89**, (2018).
17. A.M. Alamri, M.A. Wakil, P. Kwong, Z.T. Alwahabi, J. Anal. At. Spectrom. **40**, 1821 (2025)
18. R. Fantoni, S. Almaviva, L. Caneve, F. Colao, G. Maddaluno, P. Gasior, M. Kubkowska, Spectrochim. Acta B. At. Spectrosc. **129**, 8 (2017)
19. E.J. Kautz, E.C. Rönnebro, A. Devaraj, D.J. Senor, S.S. Harilal, J. Anal. At. Spectrom. **36**, 1217 (2021)
20. E.J. Kautz, A. Devaraj, D.J. Senor, S.S. Harilal, Opt. Express **29**, 4936 (2021)
21. E.J. Kautz, M.P. Polek, E.C. Rönnebro, S.S. Harilal, Spectrochim. Acta B. At. Spectrosc. **217**, 106952 (2024)
22. I. Traparic, D. Rankovic, B.D. Stankov, J. Savovic, M. Kuzmanovic, M. Ivkovic, Spectrochim. Acta B. At. Spectrosc. **221**, 107050 (2024)
23. S.S. Harilal, A.K. Shaik, E.J. Kautz, A. Devaraj, A.M. Casella, D.J. Senor, J. Anal. At. Spectrom. **39**, 699 (2024)
24. B. Schweer, A. Huber, G. Sergienko, V. Philipps, F. Irrek, H. Esser, U. Samm, M. Kempenaars, M. Stamp, C. Gowers, J. Nucl. Mater. **337**, 570 (2005)
25. M. Zlobinski, G. Sergienko, Y. Martynova, D. Matveev, B. Unterberg, S. Brezinsek, B. Spilker, D. Nicolai, M. Rasinski, S. Möller, Nucl. Mater. Energy **19**, 503 (2019)
26. M. Zlobinski, S. Brezinsek, A. Bürger, K. Dominiczak, H.G. Esser, M. Freisinger, A. Huber, C. Linsmeier, Y. Martynova, D. Nicolai, Fusion Eng. Des. **146**, 1176 (2019)
27. M. Zlobinski, G. Sergienko, I. Jepu, C. Rowley, A. Widdowson, R. Ellis, D. Kos, I. Coffey, M. Fortune, D. Kinna, Nucl. Fusion **64**, 086031 (2024)
28. S.-A. Yehia-Alexe, A. Groza, M. Serbanescu, M.E. Zarif, B. Bita, P. Dinca, B. Butoi, C. Staicu, C. Porosnicu, Spectrochim. Acta Part B At. Spectrosc. **208**, 106774 (2023)
29. S.-A. Yehia-Alexe, M. Serbanescu, P. Dinca, B. Butoi, M.E. Zarif, C. Porosnicu, A. Groza, Spectrochim. Acta B, At. Spectrosc. (2025). https://doi.org/10.1016/j.sab.2025.107197
30. S. Jovićević, M. Ivković, Z. Pavlović, N. Konjević, Spectrochim. Acta Part B At. Spectrosc. **55**, 1879 (2000)
31. S. Jovićević, M. Ivković, N. Konjević, Spectrochim. Acta Part B. At. Spectrosc. **56**, 2419 (2001)
32. N. Vujadinovic, I. Traparic, B.D. Stankov, D. Rankovic, M. Kuzmanovic, M. Ivkovic, Sci. Rep. **15**, 12589 (2025)
33. A.M. Keszler, L. Nemes, J. Mol. Struct. **695**, 211 (2004)
34. M. Hanif, M. Salik, F. Arif, Plasma Phys. Rep. **41**, 274 (2015)
35. J. Freeman, P. Diwakar, S. Harilal, A. Hassanein, Spectrochim. Acta Part B At. Spectrosc. **102**, 36 (2014)
36. S. S. Harilal, J. R. Freeman, P. K. Diwakar, and A. Hassanein, in *Laser-Induc. Breakdown Spectrosc. Theory Appl.* (Springer, 2014), pp. 143–166.
37. S. Jovičević, M. Ivković, N. Konjević, S. Popović, L. Vušković, J. Appl. Phys. **95**, 24 (2004)
38. M.A. Gigosos, M.A. Gonzalez, V. Cardenoso, Spectrochim. Acta B, At. Spectrosc. **58**, 1489 (2003)
39. S. Almaviva, L. Baiamonte, M. Pistilli, J. Nuclear Eng. **6**, 22 (2025)

Measurement Science and Technology

PAPER

RECEIVED
27 February 2026

REVISED
25 March 2026

ACCEPTED FOR PUBLICATION
31 March 2026

PUBLISHED
20 April 2026

Functional model of modular measuring head for *in situ* low pressure LIBS on complex surface geometries

M Ivković[1,*], N Vujadinović[1], I Traparić[1], B D Stankov[1], M Gavrilović-Božović[2], M Kuzmanović[3] and J Savović[4]

[1] Institute of Physics Belgrade, University of Belgrade, Pregrevica 118, 11080 Belgrade, Serbia
[2] Faculty of Engineering, University of Kragujevac, Sestre Janjić 6, 34000 Kragujevac, Serbia
[3] Faculty of Physical Chemistry, University of Belgrade, 11158 Belgrade, Serbia
[4] Vinca Institute of Nuclear Sciences, University of Belgrade, 11000 Belgrade, Serbia
[*] Author to whom any correspondence should be addressed.

E-mail: ivke@ipb.ac.rs

keywords: *in-situ* elemental analysis, modular LIBS measuring head, vacuum sealing, surface adapted spectroscopic diagnostics

Supplementary material for this article is available online

Abstract

Low-pressure laser-induced breakdown spectroscopy (LP-LIBS) offers improved spectral resolution relative to atmospheric pressure operation due to reduced line broadening and may also improve the signal-to-noise ratio (SNR). However, implementing LP-LIBS for *in-situ* material characterization presents significant technical challenges, particularly in maintaining stable LP conditions during measurements. The aim of this work is to, for the first time, present design, construction, and validation of a modular LIBS measuring head (MH) specifically engineered for *in situ* operation at reduced pressures (1–200 mbar) with adaptable sealing configurations. The system features three distinct vacuum sealing approaches, interchangeable adapters for various surface geometries, and the capability for integration with advanced plasma excitation techniques including high-voltage discharge enhancement. Experimental validation using multiple elastomer materials demonstrates effective sealing across diverse surface conditions, achieving pressures below 1 mbar on smooth surfaces and maintaining stable conditions at 10–20 mbar up to atmospheric pressure during spectroscopic measurements. Spectroscopic characterization confirms the absence of atmospheric contamination and demonstrates analytical performance comparable to conventional vacuum chamber LIBS setups. The modular design enables customization for specific analytical requirements, including spatial confinement, magnetic field application, and discharge-enhanced excitation schemes. Spectroscopic testing also revailed that the achieved SNR in the MH with CCD camera is around 3000, while realized discharge-enhanced excitation scheme caused eightfold increase in Cu I line intensities. This versatile MH addresses critical technical barriers in LP-LIBS implementation and extends the technique's applicability to challenging *in-situ* analysis scenarios across materials science, industrial diagnostics, and specialized applications requiring controlled LP environments including diagnostics of plasma facing components of fusion related reactors.

1. Introduction

Laser-induced breakdown spectroscopy (LIBS) has emerged as a powerful analytical technique for rapid, multi-element material characterization with minimal sample preparation requirements [1–6]. The technique relies on focusing a high-energy laser pulse onto a material surface, creating localized plasma through laser ablation. Spectroscopic analysis of the plasma emission enables qualitative and quantitative determination of elemental composition with high sensitivity and spatial resolution. The application scope of LIBS is vast and diverse, encompassing the analysis of soils [7], organic samples [8–10], explosives detection [11], olive oil classification [12] and many other fields.

Achieving optimal analytical performance in LIBS requires careful control and optimization of the camera recording time as well as the laser parameters (wavelength, energy, and spot size) [13–15]. Besides this, a critical parameter influencing LIBS analytical performance is the ambient gas environment, particularly the pressure at which measurements are conducted. While atmospheric pressure LIBS offers operational simplicity, numerous studies have demonstrated that LP operation (typically 1–100 mbar) provides substantial advantages [16–22]: (1) enhanced signal intensity: reduced gas pressure decreases collisional quenching of excited states, prolonging plasma emission lifetime and substantially increasing spectral line intensities [16, 17]; (2) improved signal-to-noise ratio (SNR): lower background continuum emission at reduced pressures significantly improves detection limits, particularly for trace element analysis [18, 19]; (3) superior spectral resolution: decreased pressure broadening of spectral lines enables better resolution of closely-spaced transitions, critical for isotopic analysis and complex spectral regions [20, 21]; (4) reduced matrix effects: lower pressure conditions can minimize self-absorption effects and improve calibration linearity across wider concentration ranges [22].

Despite these well-documented advantages, practical implementation of LP-LIBS faces significant technical challenges. Conventional approaches typically require placing samples inside vacuum chambers, which severely limits *in-situ* and field applications. This constraint has restricted LP-LIBS primarily to laboratory settings where samples can be transported and analyzed under controlled conditions [19, 23].

Several research groups have attempted to address this limitation through innovative instrumental designs. Portable LIBS systems operating at atmospheric pressure have been extensively developed [24], offering field deployment capabilities but sacrificing the analytical advantages of LP operation. Gas-purging methods, where controlled gas atmospheres are delivered to the measurement point through nozzles or flow cells, represent an intermediate approach [25, 26]. However, these configurations cannot achieve the optimal pressure ranges (10–20 mbar for many applications) where LP-LIBS demonstrates maximum analytical performance.

This work addresses these limitations by presenting a comprehensive solution for versatile LP-LIBS implementation: a modular measuring head (MH) designed specifically for operation at controlled low pressures (1–200 mbar) with adaptable configurations for various analytical requirements and surface geometries. The system features three distinct vacuum-sealing configurations optimized for different surface conditions and pressure requirements and a modular adapter architecture that enables measurements on diverse surface geometries and sample types. In addition, the MH is compatible with both manual operation using telescopic arms and robotic manipulation systems, and includes provisions to prevent sample contamination and memory effects through the use of replaceable protective components.

The development approach prioritized practical functionality and experimental validation. Extensive leak rate testing was conducted across various elastomer materials and surface conditions to characterize sealing performance. Spectroscopic validation confirmed the absence of atmospheric contamination under operating conditions and demonstrated analytical capabilities comparable to conventional vacuum chamber LIBS setups.

The modular LP-LIBS instrumentation presented in this work also establishes a framework that can be adapted to specialized techniques for LIBS signal amplification and consequent increase in its analytical performance. The MH architecture readily accommodates modifications for spatially-confined plasma generation [27], magnetic field application for emission enhancement [28], and integration with complementary excitation schemes such as laser-induced fast pulse discharge (LIFPD) [21, 29] or microwave-induced plasma coupling [30].

The remainder of this paper is organized as follows: section 2 describes the complete LIBS system architecture, with detailed focus on the MH design, sealing mechanisms, and system components. Section 3 presents experimental validation results, including leak rate characterization, spectroscopic verification of LP operation, and demonstration of discharge-enhanced LIBS within the MH. Section 4 discusses the implications of this work for LP-LIBS applications and outlines potential extensions of the technology. Section 5 provides concluding remarks on the significance and future directions of this development.

2. LIBS system design

The complete LP-LIBS system comprises three main components: (1) the MH, which creates and maintains the LP environment at the measurement location; (2) the main unit (MU), containing lasers, spectrometers, gas handling equipment, and control electronics; and (3) the remote control system (RC),

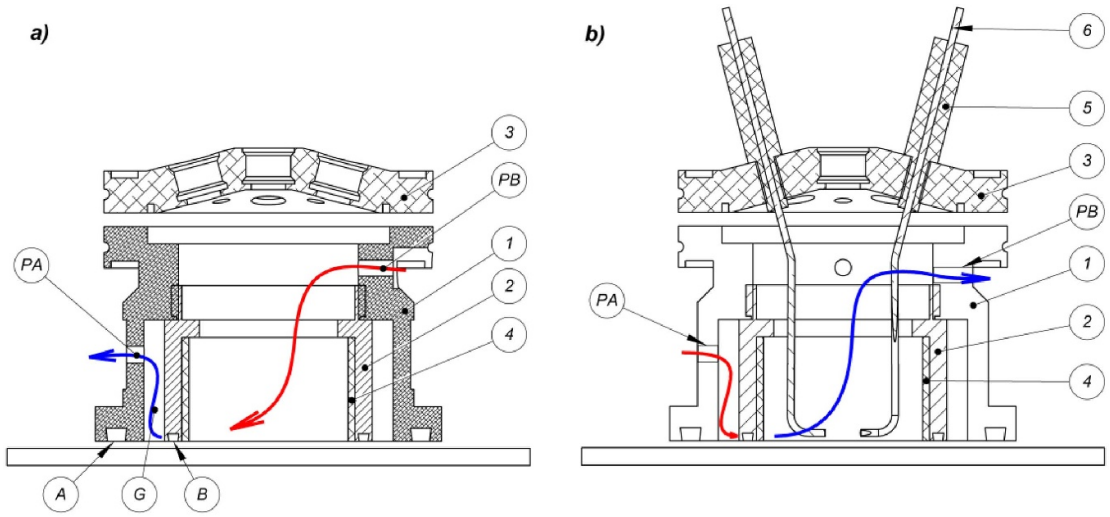

Figure 1. Measuring head cross section schematics a) without and b) with additional electrodes. Components: (1) main chamber, (2) upper body with windows and connections, (3) adapter to the component being analyzed, (4) metallic foil or isolating ring, (5) isolator, (6) electrode connections used for discharge enhanced LP operation testing, (A) space for complex shape elastomer, (B) space for O-ring, (G) groove between main chamber and adapter, while (PA) and (PB) are ports that can be used for gas inlet or vacuuming interchangebly. Vacuuming path is showed with blue arrow and gas flow is shown in red arrow.

enabling operation and monitoring. This modular architecture separates the compact, adaptable MH from the larger equipment components, facilitating flexible deployment strategies.

2.1. MH construction

The MH represents the core innovation of this work, designed specifically to create and maintain stable LP conditions during LIBS measurements without requiring sample placement in a vacuum chamber. The complete assembly consists of three primary components: the main chamber (1), the upper body with optical and connection ports (2) and the surface adapter (3), as illustrated in figure 1(a).

2.1.1. Main chamber design

The main chamber establishes the controlled LP volume for plasma generation and spectroscopic observation. In the functional prototype presented here, the internal measurement volume has dimensions of ϕ5 cm $\times$ 4.5 cm, with an outer diameter of 10 cm. This relatively compact design enables operation in confined spaces while providing sufficient volume for plasma evolution without significant wall interactions.

The chamber incorporates several critical design features: (1) protective components: a 5 mm annular rim at the upper adapter interface accommodates easily replaceable metallic foil, glass, or ceramic rings (component 4 in figure 1(a)). These protective elements serve dual purposes: (a) preventing plasma propagation to sealing components at the chamber bottom, and (b) minimizing deposition of ablated material on chamber walls that could cause memory effects and compromise measurement accuracy; (2) vacuum/gas ports: two strategically positioned ports (PA and PB) enable vacuum pumping, controlled gas supply, and pressure monitoring. The specific roles of these ports depend on the selected sealing configuration (detailed in section 2.1.3); (3) sealing grooves: a 30 mm deep, 5 mm wide primary groove (G) between the main chamber and adapter, along with two smaller grooves (A and B) at the chamber bottom, accommodate various elastomer configurations for different sealing strategies and surface conditions.

The modular design philosophy extends to dimensional scalability. For applications requiring analysis of larger or smaller components, the adapter (component 3 in figure 1(a)) can be redesigned while maintaining compatibility with the main chamber. This approach enables a single main chamber/upper body assembly to serve diverse analytical requirements through adapter exchange.

2.1.2. Upper body and optical configuration

The upper body (component 2 in figure 1(a)) is based on a standard DN63 vacuum flange and provides all optical access and auxiliary connections. The design features:

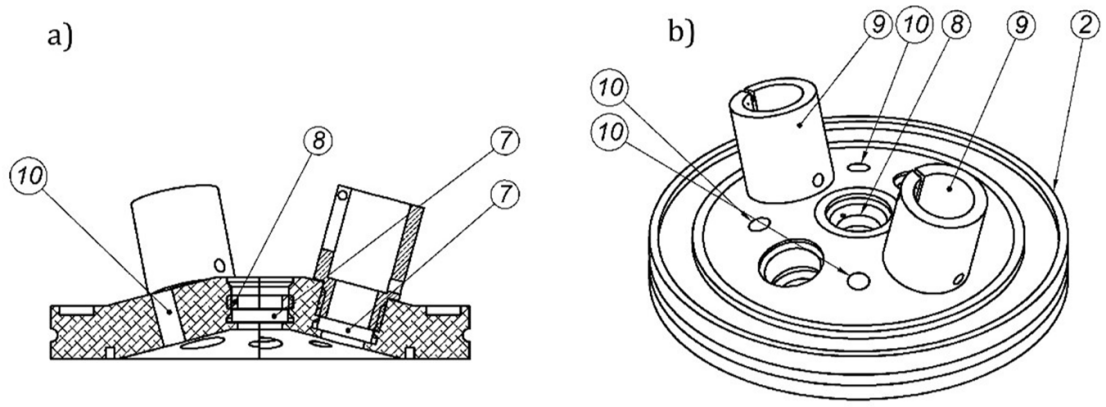

Figure 2. Upper body of the measuring head schematics: a) side view and b) perspective view. Components: (2) DN63 standard vacuum connection body, (7) laser port windows/lenses, (8) window tightening screw, (9) fiber ferrules for fiber mounting and (10) additional ports with M6 metric screw threads.

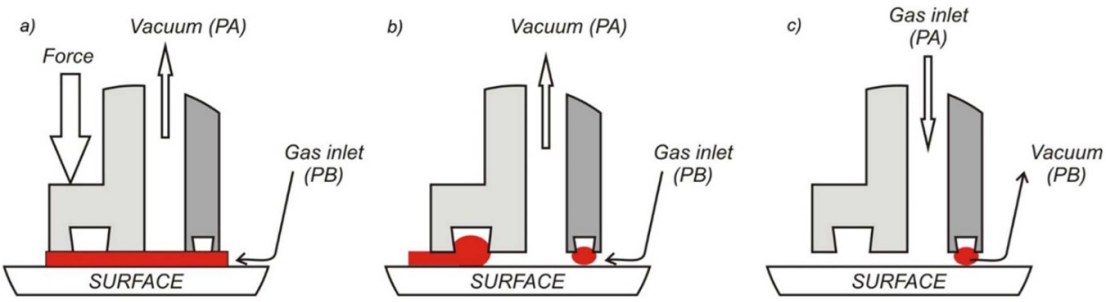

Figure 3. Versions of the measuring head main body connections to the surface: a) gasket with force applied at the edge—vacuuming inside groove—PA; b) vacuuming through big groove PA and low pressure gas supply at top of vacuum chamber—PB and c) high pressure gas through PA and big groove (gas curtain), vacuuming from the top of chamber—PB.

(1) Optical windows: five ports are distributed across the flange—one central and four radially positioned openings (components 7 in figure 2(a)). The configuration accommodates: two laser beam entry paths (enabling dual-pulse LIBS), one emission collection path, one illumination/observation path for endoscopic monitoring, and one auxiliary path for flexibility. All optical windows utilize double O-ring seals secured with screws, ensuring reliable vacuum sealing while enabling straightforward window replacement for different wavelength ranges or optical configurations.

(2) Fiber coupling: integrated ferrules (component 9 in figure 2(b)) provide secure mounting for optical fiber cables, both for laser delivery and emission collection.

(3) Auxiliary ports: four additional M6-threaded ports (components 10 in figure 2) serve multiple functions: vacuum connections, gas supply lines, high-voltage electrical feedthroughs for discharge enhancement, aiming beam entrances, or spare capacity for future modifications.

This standardized flange approach facilitates customization while maintaining compatibility with commercial vacuum components and optical mounts.

2.1.3. Sealing configurations and operating modes

The MHs versatility stems from three distinct sealing configurations, each optimized for specific pressure requirements and surface conditions. All configurations maintain the same main chamber geometry while varying the sealing approach and gas flow patterns.

Configuration A: simple gasket sealing (figure 3(a))

This configuration employs a thin elastomeric gasket (highlighted in red in **figure 3(a)**) with inner diameter exceeding 50 mm and outer diameter up to 100 mm. The gasket directly contacts the component surface, creating a seal sufficient for operation at moderate pressures (10–100 mbar) or when using inert gas atmospheres where minor air infiltration is tolerable. Mechanical pressure applied to the MH

(indicated by arrow in figure 3(a)) compresses the gasket against the surface. Port PB supplies the working gas while port PA connects to vacuum pump. This straightforward approach works well for relatively smooth, non-porous surfaces and applications not requiring ultra-low pressure or high atmospheric purity.

***Configuration B: differential pressure sealing (*figure 3(b))**
This advanced configuration addresses analysis of rough or moderately irregular surfaces while maintaining LP capability. The design utilizes two independent sealing zones with differential pressure control:

(1) Outer seal (groove A): a specially-shaped elastomer 118 × 83 × 8.5 mm, (see section 2.1.4 and figure 3 in supplementary material for details) prevents atmospheric air ingress and working gas egress. This primary seal accommodates surface irregularities through both material compliance and extended contact length.

(2) Inner seal (groove B): a standard O-ring limits gas flow from the measurement chamber interior without directly contacting the analyzed surface. This configuration maintains a pressure gradient: atmospheric outside, intermediate in groove G, and controlled low pressure in the measurement chamber.
Continuous evacuation through the primary groove G (via port PA) removes any leaked atmospheric gas before it reaches the measurement volume. Working gas supplied through port PB establishes the desired pressure in the measurement chamber.

This configuration proved essential for irregular surfaces where simple gasket sealing could not achieve adequate vacuum, as demonstrated in section 3.1.

***Configuration C: gas Curtain Sealing (*figure 3(c))**
For applications requiring atmospheric isolation without ultra-low pressure, or when surface contact must be minimized, this configuration employs controlled gas overpressure.

Gas supplied through port PA at pressure slightly exceeding atmospheric creates an outward flow that prevents air ingress while the inner O-ring (groove B) limits gas flow into the measurement chamber. The mass flow controller-manometer feedback loop maintains constant chamber pressure despite continuous gas consumption.

This approach minimizes contact with the analyzed surface and enables operation on delicate or contamination-sensitive materials. The configuration is particularly suitable for applications requiring inert atmospheres at moderate pressures (10–200 mbar) rather than high vacuum conditions.

The insertion of the working gas can be realized through additional ports of the upper body of the MH (components 10 in figure 2(b)).

Adapter customization
For components with geometries incompatible with the standard MH interface, custom adapters (component 3 in figure 1(a)) can be fabricated. The modular design enables adapter shapes conforming to complex surface geometries, including non-circular cross-sections matching rectangular or irregular component shapes, curved bottom surfaces conforming to cylindrical or complex curvatures, extended or reduced height profiles for optimal positioning relative to optical paths or integrated features for specialized plasma confinement or excitation schemes.

The adapter's upper portion maintains standardized threading for attachment to the main chamber, while the lower section is customized for the specific application. This approach provides maximum flexibility without requiring multiple complete MH assemblies.

2.1.4. elastomer requirements and selection
Effective vacuum sealing across diverse surface conditions requires careful elastomer material selection and geometric optimization. The performance of LP-LIBS measurements depends critically on achieving and maintaining the target pressure range, making seal quality a dominant factor in system capability.

Material selection must balance multiple factors such as operating temperature range (room temperature to ∼100 °C for LIBS applications), pressure differential capabilities (1–1000 mbar differential), chemical compatibility with working gases and potential contaminants, surface conformability and recovery properties, long-term stability and compression set resistance, as well as assembly and maintenance requirements.

Elastomer geometries
Two distinct geometries serve different sealing functions:

(1) Inner seal (groove B): standard O-rings (in this implementation) provide reliable restriction of gas flow into the measurement volume. The circular cross-section offers excellent sealing with minimal contact force, reducing potential for surface damage or contamination.

(2) Outer seal (groove A): a custom complex profile (detailed design in supplementary material) optimizes two critical functions: adequate filling of the groove depth to establish primary containment, and extended 'tail' section providing prolonged surface contact to enhance sealing capacity despite surface irregularities.

This specialized geometry cannot be produced from standard O-ring stock. A custom manufacturing tool was developed to fabricate these seals from various elastomer materials, enabling systematic testing and optimization.

Elastomer materials
Four elastomer materials were evaluated for sealing performance:

- Silicone rubber (Q): 40 Shore A hardness—excellent flexibility and recovery
- Natural rubber (NR): 45 and 55 Shore A hardness—good general-purpose properties
- Nitrile butadiene rubber (NBR): 70 Shore A hardness—superior chemical resistance

Comprehensive leak rate testing (section 3.1) revealed that hardness is a dominant parameter for rough surface applications, with the 70 Shore NBR providing optimal performance. For porous surfaces, the softer 40 Shore silicone demonstrated advantages through enhanced conformability. All sealing components use the same 118 × 83 × 8.5 mm dimensions for consistency.

Detailed drawings, photographs of manufactured seals, and the fabrication tool design are provided in the supplementary material.

2.2. MU and system integration for *in-situ* operation

While the MH constitutes the primary innovation, the complete LP-LIBS system for *in-situ* operation will require integrated support equipment for operation. MU should house all components except the MH itself, enabling either centralized operation from a control room or field deployment on a mobile cart.

2.2.1. Essential equipment components

Essential equipment encompases:

Laser System: One or two Q-switched Nd:YAG lasers (for single or dual-pulse LIBS) with power supplies, beam conditioning optics, and fiber coupling assemblies. The optical train includes beam expanders, spatial filters, and precision alignment mechanisms for efficient fiber coupling while preventing fiber damage (discussed in section 2.2.2).

Detection system: spectrometer(s) equipped with intensified CCD and/or standard CCD cameras, depending on temporal resolution requirements. For applications requiring high spectral resolution ($R > 20\,000$), echelle spectrometers provide optimal performance. Segmented spectrometers offer advantages for surveys requiring broad spectral coverage.

Fiber optic coupling: F-matcher optics transfer emission from collection fibers to spectrometer entrance slits with appropriate magnification and illumination characteristics.

Gas handling: mass flow controllers, pressure gauges (capacitive manometers for accuracy at low pressure), and control electronics maintain target pressure with feedback regulation. Small gas cylinders (1–2 l) provide sufficient capacity for extended operation given the low flow rates required.

Vacuum system: compact rotary vane pump (15 $m^3\ h^{-1}$ capacity sufficient for this application) with valves and pressure monitoring.

Power supply systems: AC mains distribution and DC power supplies for all subsystems. Optional high-voltage DC supply and storage capacitors for discharge-enhanced LIBS modes.

Advanced options: microwave generators for coupled laser ablation/microwave-induced plasma techniques [30], additional discharge power supplies for alternative excitation modes.

Data acquisition and control: computer system with camera interfaces, spectrometer control software, data analysis capabilities, and process control for gas handling and safety interlocks.

2.2.2. Fiber optic considerations for laser delivery

Transmitting high-energy laser pulses through optical fibers presents significant technical challenges due to fiber damage thresholds. Published studies demonstrate permanent damage to hard-clad silica and plastic-clad-silica fibers at energies as low as few mJ [31]. For the typical pulse energies required for LIBS (50–200 mJ), two approaches enable safer fiber transmission:

(1) Low-energy operation: core diameters $\geqslant$600 µm with careful coupling optics enable transmission of 20–50 mJ pulses suitable for many LIBS applications [32–35].

(2) Hollow-core fibers: gas-filled hollow waveguides tolerate higher energies through reduced interaction with solid material [36]. Gas circulation through the fiber bore provides cooling and prevents damage accumulation.

All fiber coupling systems incorporate precision *x*–*y*–*z* positioning stages for optimal beam alignment and diverging beam geometry (focus position before fiber entrance) to prevent air breakdown at the coupling interface.

2.2.3. RC and monitoring

The RC system provides wireless communication between the MH location and operator station, essential for applications where direct line-of-sight is unavailable or operator presence near the measurement point is undesirable.

Video monitoring: endoscopic camera system with integrated LED illumination enables real-time observation of the measurement area, target surface, and plasma generation. The compact camera (7 mm diameter) with 5 m light guide provides adequate resolution (640 × 480 pixels) for targeting and process monitoring.

System status: wireless displays show critical parameters including pressure, gas flow rates, laser energy, and spectral acquisition status.

Safety interlocks: remote emergency shutdown capability and automated safety responses to fault conditions (pressure loss, laser interlock violations, etc).

The complete system architecture enables flexible operation modes: fully automated sequences for routine measurements, manual control for method development and optimization, or hybrid approaches combining automated measurement protocols with operator oversight.

3. Experimental validation

Experimental testing validated three critical aspects of the MH performance: (1) sealing effectiveness across various surface conditions and elastomer materials, (2) spectroscopic verification of LP operation without atmospheric contamination, and (3) analytical capabilities including advanced excitation modes. These evaluations establish the practical functionality of the proposed LP-LIBS configuration.

3.1. Sealing performance and leak rate characterization

Quantitative assessment of sealing performance provides essential data for optimizing elastomer selection and predicting operational capabilities across diverse surface conditions.

The MH was connected to a rotary vane vacuum pump (Alcatel 2012 A, 15 $m^3\ h^{-1}$ pumping speed) through both PA and PB ports (Configurations A, B and C from figure 3). Pressure was monitored with a Leybold Heraeus DV 1000 manometer.

Table 1. Experimental testing of different elastomers leak rates.

Elastomer type	Surface	Time (s)	Leak rate(mbar cm^3 s^{-1})
Silicone rubber(Q, 40 Shore A)	Stone	90	9.7
	Rough metal	270	3.2
	Wood varnished	300	2.9
	Polished metal	330	2.6
Nitrile butadiene rubber(NBR, 70 Shore A)	Stone	10	87.0
	Wood varnished	310	2.8
	Rough metal	315	2.8
	Polished metal	330	2.6

Validation testing with a soft rubber gasket in configuration A (figure 3(a)) demonstrated that pressures below 1 mbar were achieved using either port for vacuum pumping, confirming adequate sealing performance. Mechanical pressure was applied initially and was no longer required once low pressure was reached.

In configuration B (figure 3(b)), after evacuating to <0.1 mbar, a needle valve isolated the MH from the pump and pressure evolution was monitored. The time required for pressure to increase from 0.1 to 10 mbar characterized the leak rate for each surface/elastomer combination. Leak rate was calculated as $Q = \mathrm{V} \cdot \mathrm{d}P/\mathrm{d}t$, where V denotes the volume of the MH and $\mathrm{d}P/\mathrm{d}t$ is the rate of change of pressure (here fixed to 9.9 mbar). Test surfaces included stone (porous, rough), varnished wood (non-porous, smooth), rough machined metal and polished metal.

Table 1 presents leak rates for silicone rubber (Q, 40 Shore A) and nitrile butadiene rubber (NBR, 70 Shore A) used in configuration B (figure 3(b)). The two natural rubber formulations (45 and 55 Shore A) showed performance within experimental uncertainty of these values and are not separately tabulated. Key findings can be summarized as follows:

(1) *Surface hardness dominance:* for rough, non-porous surfaces (rough metal, varnished wood, polished metal), the harder NBR (70 Shore) demonstrated equal or slightly better sealing with leak rates 0.27–0.29 bar cm^3 s^{-1} compared to 0.27–0.33 bar cm^3 s^{-1} for silicone.

(2) *Porous surface exception*: on porous substrate (stone), the softer silicone rubber (40 Shore) performed markedly better, with leak rates around 10 times lower than NBR. The enhanced conformability of softer elastomers enables penetration into surface porosity for improved sealing.

(3) *Pump capacity validation:* the measured leak rates confirmed that continuous pumping at 15 m^3 h^{-1} capacity maintains stable LP conditions even on moderately rough surfaces. These results guided subsequent spectroscopic testing, with NBR 70 Shore selected for smooth and rough metal surfaces (most relevant for typical LIBS applications) and silicone 40 Shore reserved for porous materials.

Configuration C (figure 3(c)) was tested to determine whether argon flow through port PA disrupts the pressure established in the vacuum chamber, which is evacuated through port PB. The test surfaces included rough machined metal and stone. The lowest pressures achieved prior to initiating the argon gas curtain were 12 mbar for the rough-machined metal and 14 mbar for the stone surface. After initiation of the argon flow at 25 l min^{-1}, corresponding to an overpressure of 130 mbar above atmospheric pressure, the pressure inside the vacuum chamber remained unchanged for both test surfaces. These results demonstrate that configuration C can achieve and maintain low pressures suitable for LIBS applications while effectively preventing the ingress of ambient gas.

3.2. Spectroscopic verification of LP operation

Beyond mechanical leak rate measurements, spectroscopic analysis provides definitive confirmation that the MH maintains atmospheric isolation during plasma generation and emission collection.

Figure 4 illustrates the complete system used for spectroscopic testing. The laser source was a Quantel QSmart 450 Nd:YAG laser operating at the fundamental wavelength of 1064 nm, with a maximum energy of 450 mJ, pulse duration of 6 ns, repetition rate of 10 Hz, beam diameter of 6 mm, and divergence below 0.5 mrad. The laser beam was focused using a plano-convex lens with a focal length of 100 mm, positioned 90 mm from the target surface, producing an approximately 1 mm diameter focal spot with fluence sufficient for reliable plasma generation on copper targets. Copper samples were mounted on precision positioning stages consisting of computer-controlled *XY* stepper motors and

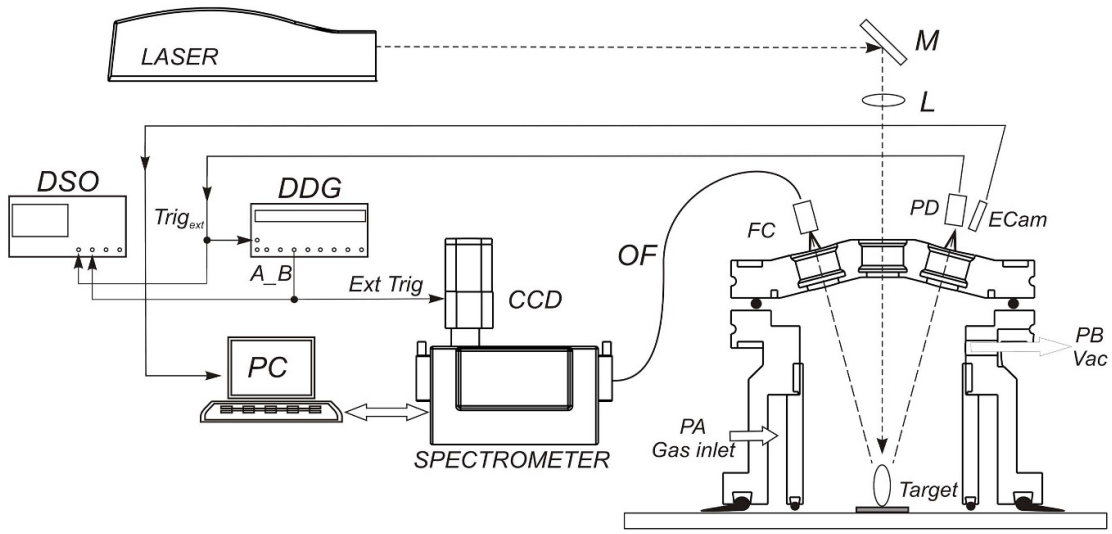

Figure 4. Experimental setup used for the spectroscopic testing of the MH functional model. Components: M—mirror, L—focusing lens, FC—collimator, OF—optical fiber, DDG—digital delay generator, DSO—digital storage oscilloscope, PD—photodiode, ECam—endoscopic camera.

a pitch/roll platform, enabling fresh surface exposure for each measurement sequence. The MH was mounted on a flat rough steel plate and evacuated using Configuration B (figure 3(b)), while a continuous helium flow maintained a stable low pressure during measurements. Plasma emission was collected by a collimator (FC) and guided via an round to linear optical fiber (core diameter Ø400 μm, NA 0.22, 99% transmission efficiency in wavelength range of interest) to the entrance slit of the spectrometer. Detection was performed using a SOL Instruments MS7504i imaging spectrometer equipped with a 1200 l mm^{-1} grating (wavelength resolution 0.03 nm at blaze wavelength with 20 μm entrance slit and 12 μm pixel size CCD camera) and a Proscan HS 101 H CCD camera (2048 × 506, pixel size 12 × 12 μm, Peltier cooling, minimum gate width 1 ms) cooled down to −10 °C, with full spectral coverage from 350 to 780 nm achieved by sequential grating rotation. Real-time monitoring of plasma generation and target surface condition was provided by an endoscopic camera with a resolution of 640 × 480 pixels, six LED illumination, and a 5 m light guide.

The system was operated at a laser energy of $E = 179 \pm 2$ mJ and wavelength $\lambda = 1064$ nm. The spectrometer slit width was set to 50 μm. Camera requested a trigger TTL signal of 5 V amplitude and minimum width of 20 μs, hence the triggering was controlled by controlled by a digital delay generator (DDG), while a delay time of 1 μs and a gate width of 1 ms were set. The helium pressure was 10 mbar for full spectral measurements, while for pressure-dependence studies it was varied between 2 and 40 mbar.

The recorded complete spectrum (figure 5(a)) exhibits strong copper emission lines throughout the 350–700 nm range, with Cu I multiplets at 510.6, 515.3 and 521.8 nm showing highest intensity. The helium working gas is barely detectable (He I line at 587.6 nm shows intensity more than 20 times weaker than copper lines). Most significantly, hydrogen Balmer lines are completely absent, confirming effective exclusion of atmospheric moisture.

No emission from the aluminum alloy chamber walls was detected, verifying that plasma dimensions and energy remain confined to the target region without wall interactions that could cause contamination or memory effects.

Examination of the 740–785 nm region (figure 5(b)) reveals that the strongest oxygen emission line from the multiplet at around 777 nm is hardly distinguishable from the noise, while strong nitrogen emission lines around 740 nm are completely absent and remain below the detection limit. These observations confirm that Configuration B sealing (figure 3(b)) effectively prevents atmospheric ingress even during continuous plasma generation. Any leaked atmospheric gases are removed through the differential pumping groove G before reaching the measurement chamber.

For the pressure-dependence investigation, copper resonance line intensity and profile were measured across the 2–40 mbar pressure range in helium (figure 6). The pressure was controlled with reducing valve and additionally needle valve before the MH. Pressure was monitored also with DV 1000 manometer with overall 15% measurement error. During the measurements, the pressure did not show any significant fluctuations.

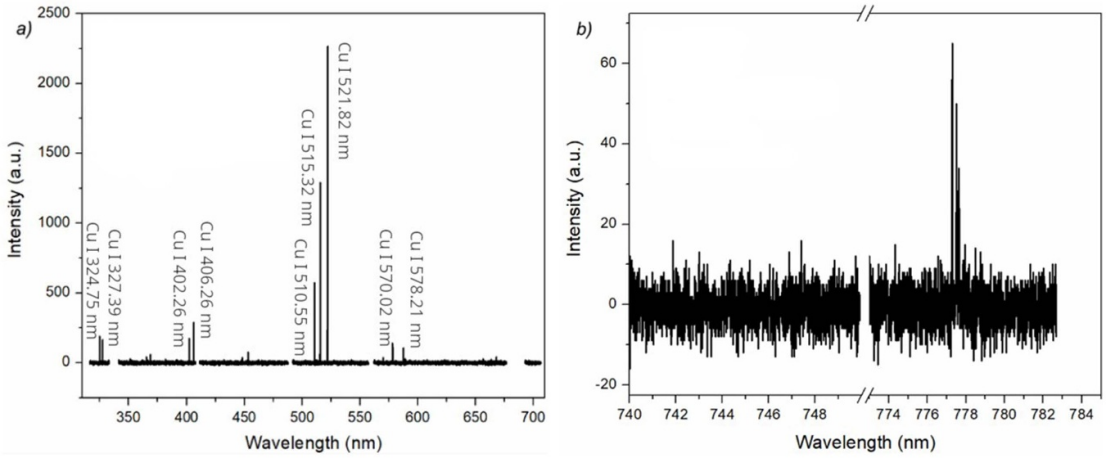

Figure 5. (a) The spectrum of the copper target recorded inside the MH and (b) region of spectrum with strongest nitrogen and oxygen lines.

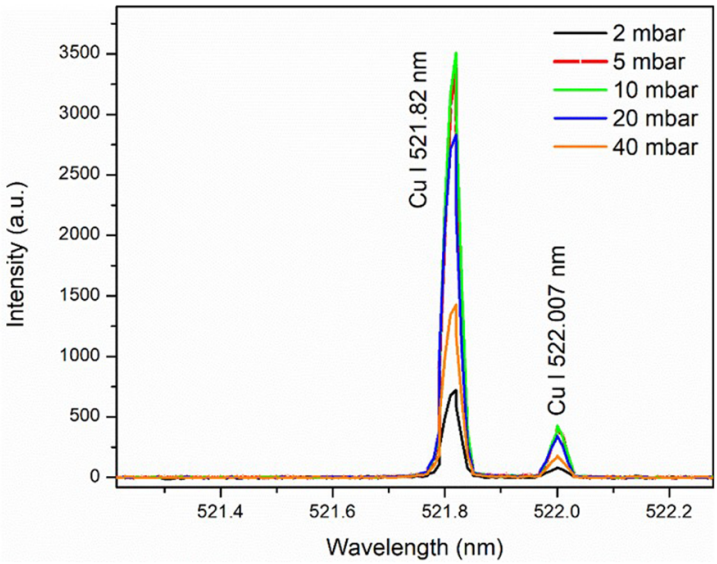

Figure 6. Recordings of Cu I lines at various pressures of helium atmosphere.

The results demonstrate nearly identical analytical characteristics to conventional vacuum chamber LIBS:

- Signal intensity maximizes at 10–20 mbar, consistent with prior studies [19].
- Line shapes and relative intensities match reference chamber measurements.
- Reproducibility (relative standard deviation) <5% across 10-shot averages.

These results validate that the MH introduces no significant analytical artifacts compared to standard vacuum chamber configurations, while enabling in-situ measurement capability.

3.3. Discharge-enhanced LIBS in MH

The modular adapter design enables integration of electrodes for LIFPD, potentially enhancing emission intensity and improving detection limits. This capability was validated by incorporating a custom electrode assembly in adapter component 3 from figure 1(b).

Two electrodes are positioned 4 mm apart, located 6 mm above the target surface. High-voltage connection via auxiliary port on upper body (component d in figure 2). Photographs of the electrode assembly without discharge operation appear in the supplementary material.

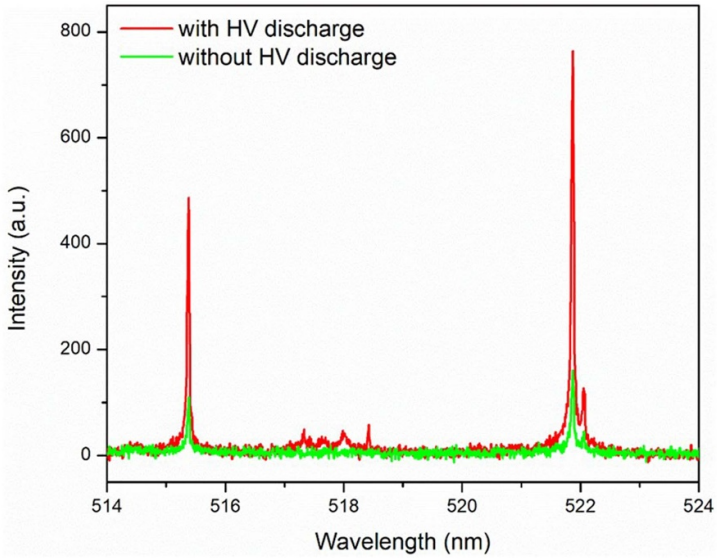

Figure 7. Comparison of intensities of Cu I lines at 515.3 nm and 521.8 nm in air at atmospheric pressure obtained with LIFPD (red) and LIBS (green).

Experimental measurements were performed at atmospheric pressure in air. Capacitors with 100 nF capacitance were charged to 5 kV and discharged through the laser-induced plasma. Comparison of LIBS (laser only) versus LIFPD (laser and discharge) spectra is given in figure 7. An eightfold increase in Cu I line intensities was observed, as well as improved SNR and extended temporal emission window. The additional discharge may introduce local pressure variations within the discharge zone. However, such effects are not of particular importance to the analytical performance of the method, since these variations would not cause significant changes in electron density to broaden the lines of interest and decrease analytical performance compared to atmospheric LIBS or LP-LIBS.

Previous work [29] demonstrated three-fold SNR enhancement and five-fold intensity increase for rhenium detection in tungsten using LIFPD at low pressure. Our MH configuration for the first time enables straightforward implementation of this technique for applications requiring enhanced sensitivity.

The adapter architecture of the MH provides accommodations for other excitation modes such as magnetic field application for Zeeman-based diagnostics, spatial confinement structures for plasma shaping, microwave coupling for laser ablation-microwave induced plasma combination [30] and glow discharge electrodes for alternative ionization schemes. This versatility significantly expands the MH's analytical capabilities beyond conventional LIBS.

4. Discussion

The experimental validation results demonstrate that the proposed MH successfully achieves the primary design objectives: creating and maintaining stable LP environments for LIBS measurements without requiring sample placement in vacuum chambers. This capability addresses a significant limitation that has restricted LP-LIBS predominantly to laboratory settings with transportable samples.

4.1. Analytical performance comparison

The spectroscopic validation (section 3.2) reveals that LIBS plasma generated within the MH exhibits analytical characteristics nearly identical to conventional vacuum chamber configurations. This equivalence confirms that the compact geometry, optical window configuration, and sealing approach do not introduce detrimental artifacts. The MHs demonstrated capabilities include:

- Effective atmospheric isolation (oxygen lines barely distinguishable from the noise, nitrogen below detection limits)
- Pressure-dependent behavior matching reference studies

- Reproducibility comparable to laboratory vacuum systems
- Integration compatibility with advanced excitation modes

For applications where these analytical capabilities meet requirements, the MH enables LP-LIBS measurements previously impractical or impossible.

4.2. Versatility through modular design

The three sealing configurations (section 2.1.3) address diverse measurement scenarios providing cost-effective customization for specialized applications:

(1) *Configuration A (simple gasket)*: suitable for smooth surfaces and applications tolerating minor atmospheric ingress. Minimal complexity enables rapid deployment and reliable operation.

(2) *Configuration B (differential pressure):* optimized for rough or irregular surfaces requiring low pressure and complete atmospheric isolation. Continuous differential pumping removes leaked gases before they reach the measurement volume, enabling reliable operation on challenging surfaces.

(3) *Configuration C (gas curtain):* designed for delicate surfaces where mechanical contact must be minimized, or moderate pressure inert atmospheres suffice. Outward gas flow prevents substantial atmospheric ingress while reducing contact forces.

The interchangeable adapter approach (component 3, figure 1) extends versatility to diverse sample geometries without requiring multiple complete MH assemblies. Custom adapters accommodate non-standard cross-sections (rectangular, complex shapes), curved surfaces (matching component curvature), specialized plasma confinement geometries and integration of electrodes, magnets, or other enhancement structures.

4.3. Technical limitations and considerations

While the MH demonstrates substantial capabilities, several limitations and practical considerations merit discussion:

Achievable pressure range: leak rate characterization (table 1) shows that surface condition fundamentally determines the minimum achievable pressure. Smooth, non-porous surfaces enable operation below 1 mbar with simple gasket sealing, while rough surfaces require differential pressure sealing and typically limit operation to 10–50 mbar even with continuous pumping. Applications requiring ultra-high vacuum ($<10^{-3}$ mbar) remain restricted to conventional vacuum chambers.

Surface contact requirements: all demonstrated configurations require some degree of contact between elastomer seals and the analyzed surface. This contact may be unacceptable for certain delicate or contamination-sensitive materials, despite the gas curtain configuration minimizing contact forces.

Measurement volume constraints: the compact chamber geometry (ϕ5 cm $\times$ 4.5 cm interior in this implementation) restricts plasma expansion compared to large vacuum chambers. While spectroscopic validation showed no adverse effects for copper target analysis at 10 mbar, applications involving highly energetic plasmas or large ablation craters may encounter wall interactions. Chamber dimensions can be scaled up, but maintaining effective sealing becomes increasingly challenging.

Optical window access: the fixed optical port configuration (two laser entry, one emission collection, one observation, one auxiliary) provides excellent versatility but may constrain specialized geometries requiring, for example, multiple simultaneous emission collection angles or complex beam delivery configurations.

4.4. Applications beyond conventional LIBS

The MH architecture for the first time enables several advanced analytical approaches:

LIFPD: demonstrated intensity enhancement (section 3.3) provides improved detection limits for trace element analysis. Previous studies showed particular advantages for detecting low concentrations in complex matrices [21, 29].

Spatially-confined LIBS: custom adapters incorporating confinement structures can exploit plasma compression effects for emission enhancement [27].

Magnetic field application: integrated magnets enable magnetic field enhanced LIBS [28].

Hybrid techniques: the modular design accommodates combinations of laser ablation with alternative excitation/ionization schemes (microwave-induced plasma [30], glow discharge, arc discharge), potentially expanding analytical capabilities beyond pure LIBS.

These advanced capabilities position the MH as a versatile platform for LP-LIBS research and specialized applications.

4.5. Future development directions

Several extensions of this work could further enhance capabilities:

Automated Positioning: integration with robotic manipulation systems or motorized arms would enable systematic multi-point surveys and automated operation in hazardous or inaccessible environments.

Real-time pressure/composition feedback: incorporating residual gas analysis or optical emission monitoring could provide continuous verification of atmospheric isolation and enable adaptive control for challenging sealing conditions.

Alternative laser wavelengths: the current optical windows accommodate visible and near-IR wavelengths. Substituting ZnSe windows would enable CO2 laser operation, potentially beneficial for isotopic analysis requiring reduced plasma electron density [20].

Miniaturization studies: investigating scaling limits could determine minimum practical measurement volumes, potentially enabling incorporation into even more constrained geometries.

Field deployment validation: systematic testing in representative application environments (industrial settings, field sites, specialized facilities) would identify practical deployment challenges and opportunities for design refinement.

5. Conclusion

This work presents a comprehensive solution for versatile LP LIBS implementation through a modular MH design specifically engineered for operation at controlled reduced pressures (1–200 mbar) without requiring sample placement in vacuum chambers. The system addresses critical technical barriers that have limited LP-LIBS predominantly to laboratory applications with transportable samples.

The effective sealing across diverse surface conditions was demonstrated, with quantified leak rates guiding the elastomer selection and sealing strategy optimization. Three distinct configurations are introduced to address different pressure requirements and surface challenges.

Spectroscopic testing's confirmed atmospheric isolation and analytical performance comparable to conventional vacuum chamber LIBS. The MH introduced no significant analytical artifacts while enabling *in-situ* measurement capability.

Finally, the integration compatibility with advanced excitation schemes was also shown. Additional fast pulse discharge yielded eightfold analyte emission enhancement within the MH.

The modular architecture based on interchangeable adapters provides cost-effective customization for specialized applications, sample geometries, and analytical requirements. This versatility extends beyond conventional LIBS to encompass hybrid techniques combining laser ablation with alternative excitation/ionization schemes.

By enabling practical implementation of LP-LIBS in diverse application scenarios, this development expands the technique's utility across materials science, industrial process monitoring, field analysis, and specialized applications requiring controlled LP environments for optimal analytical performance. The established design framework provides a foundation for continued advancement of LP-LIBS instrumentation tailored to specific analytical challenges.

Acknowledgments

The research was funded by the Ministry of Science, Technological Development and Innovations of the Republic of Serbia, Contract numbers: 451-03-47/2023-01/200024, 451-03-47/2023-01/200017, 451-03-47/2023-01/200146, 451-03-66/2024-03/200107 and by the Science Fund of the Republic of Serbia through NOVA2LIBS4fusion project Grant No. 7753287 within call IDEAS. This work was carried out

under the project: NIFS21KLPF087. We acknowledge Stanko Milanović, our technical associate, who drew all schematic figures of the measuring head. Artificial intelligence tools were used only to assist with grammar and improve the clarity and flow of the manuscript.

Data availability statement

All data that support the findings of this study are included within the article (and any supplementary files).

Measuring head photos available at https://doi.org/10.1088/1361-6501/ae59a6/data1.

Author contributions

M Ivković 0000-0003-4421-0002
Conceptualization (lead), Funding acquisition (lead), Methodology (lead), Supervision (lead), Writing – original draft (lead)

N Vujadinović 0009-0004-4415-0307
Formal analysis (equal), Investigation (equal), Writing – review & editing (equal)

I Traparić 0000-0001-6492-2360
Formal analysis (equal), Investigation (equal), Visualization (equal), Writing – review & editing (equal)

B D Stankov 0000-0002-6437-4015
Investigation (equal), Writing – review & editing (equal)

M Gavrilović-Božović
Writing – review & editing (equal)

M Kuzmanović 0000-0003-4731-7518
Writing – review & editing (equal)

J Savović
Writing – review & editing (equal)

References

[1] Miziolek A W, Palleschi V and Schechter I 2006 *Laser Induced Breakdown Spectroscopy* (Cambridge University Press)
[2] Cremers D A and Radziemski L J 2013 *Handbook of Laser-Induced Breakdown Spectroscopy* (Wiley)
[3] Noll R 2011 *Laser-Induced Breakdown Spectroscopy, in Laser-Induced Breakdown Spectroscopy: Fundamentals and Applications* (Springer)
[4] Musazzi S and Perini U 2014 *Laser-induced Breakdown Spectroscopy, Springer Series in Optical Sciences* vol 182 (Springer) p E1
[5] Singh J P and Thakur S N (eds) 2020 *Laser-Induced Breakdown Spectroscopy* 2nd edn (Elsevier)
[6] Hahn D W and Omenetto N 2010 Laser-induced breakdown spectroscopy (LIBS), part I: review of basic diagnostics and plasma—particle interactions: still-challenging issues within the analytical plasma community *Appl. Spectrosc.* **64** 335A
[7] Shirvani-Mahdavi H and Shafiee P 2016 Quantitative analysis of soil calcium by laser-induced breakdown spectroscopy using addition and addition-internal standardizations *Meas. Sci. Technol.* **27** 125502
[8] Marković M *et al* 2024 Application of laser-induced breakdown spectroscopy for the analysis of pig bones *Meas. Sci. Technol.* **35** 025502
[9] Tawfik W, Farooq W A and Alahmed Z A 2014 J *Opt. Soc. Korea* **18** 50–54
[10] Jarota A *et al* 2019 Exploring the ultrafast dynamics of a diarylethene derivative using sub-10 fs laser pulses *Phys. Chem. Chem. Phys.* **21** 192–204
[11] Kumar Myakalwar A, Spegazzini N, Zhang C, Kumar Anubham S, Dasari R R, Barman I and Kumar Gundawar M 2015 Less is more: avoiding the LIBS dimensionality curse through judicious feature selection for explosive detection *Sci. Rep.* **5** 13169
[12] Gyftokostas N, Stefas D, Kokkinos V, Bouras C and Couris S 2021 Laser-induced breakdown spectroscopy coupled with machine learning as a tool for olive oil authenticity and geographic discrimination *Sci. Rep.* **11** 5360
[13] Fikry M, Tawfik W and Omar M M 2021 Controlling the plasma electron number density of copper metal using NIR picosecond laser-induced plasma spectroscopy *Opt. Appl.* **51** 365–74
[14] Fikry M, Tawfik W and Omar M 2020 Measurement of the electron temperature in a metallic copper using ultrafast laser-induced breakdown spectroscopy *J. Russ. Laser Res* **41** 484–90
[15] Campos D, Harilal S S and Hassanein A 2010 The effect of laser wavelength on emission and particle dynamics of Sn plasma *J. Appl. Phys.* **108** 113305
[16] Effenberger J A J and Scott J R 2010 Effect of atmospheric conditions on LIBS spectra *Sensors* **10** 4907
[17] Ş Y, Tsui Y Y and Fedosejevs R 2004 Pressure dependence of emission intensity in femtosecond laser-induced breakdown spectroscopy *J. Anal. At. Spectrom.* **19** 1295
[18] Kautz E J, Rönnebro E C, Devaraj A, Senor D J and Harilal S S 2021 Detection of hydrogen isotopes in Zircaloy-4 via femtosecond LIBS *J. Anal. At. Spectrom.* **36** 1217

[19] Ivkovic M, Savovic J, Stankov B D, Kuzmanovic M and Traparic I 2024 LIBS depth-profile analysis of W/Cu functionally graded material *Spectrochim. Acta B* **213** 106874
[20] Traparic I, Rankovic D, Stankov B D, Savovic J, Kuzmanovic M and Ivkovic M 2024 Resolving studies of Balmer alpha lines relevant to the LIBS analysis of hydrogen isotope retention *Spectrochim. Acta B At. Spectrosc.* **221** 107050
[21] Stankov B, Traparić I, Božović M G and Ivković M 2025 Detection of absorbed neutrons through determination of rhenium content in tungsten with laser induced fast pulse discharge *Fusion Eng. Des.* **215** 114943
[22] Hao Z, Liu L, Shen M, Yang X, Li K, Guo L, Li X, Lu Y and Zeng X 2016 Investigation on self-absorption at reduced air pressure in quantitative analysis using laser-induced breakdown spectroscopy *Opt. Express* **24** 26521
[23] Palleschi V 2017 If laser-induced breakdown spectroscopy was a brand: some market considerations *Spectrosc. Eur.* **29** 6–9
[24] Rakovský J, Čermák P, Musset O and Veis P 2014 A review of the development of portable laser induced breakdown spectroscopy and its applications *Spectrochim. Acta B* **101** 269
[25] Senesi G S, Harmon R S and Hark R R 2020 *Field-portable and Handheld LIBS Laser-Induced Breakdown Spectroscopy* (Elsevier) pp 537
[26] Almaviva S *et al* 2020 LIBS measurements inside the FTU vessel mock-up by using a robotic arm *Fusion Eng. Des.* **157** 111685
[27] Hao Z, Deng Z, Liu L, Shi J and He X 2022 Spatial confinement effects of laser-induced breakdown spectroscopy at reduced air pressures *Front. Optoelectron.* **15** 17
[28] Akhtar M, Jabbar A, Mehmood S, Ahmed N, Ahmed R and Baig M 2018 Magnetic field enhanced detection of heavy metals in soil using laser induced breakdown spectroscopy *Spectrochim. Acta B* **148** 143
[29] Vinić M and Ivković M 2014 Spatial and temporal characteristics of laser ablation combined with fast pulse discharge *IEEE Trans. Plasma Sci.* **42** 2598
[30] Vujadinovic N, Traparic I, Stankov B D, Rankovic D, Kuzmanovic M and Ivkovic M 2025 Hydrogen isotopes retention studies using laser and microwave induced plasma coupling *Sci. Rep.* **15** 12589
[31] Allison S, Gillies G, Magnuson D and Pagano T 1985 Pulsed laser damage to optical fibers *Appl. Opt.* **24** 3140
[32] Dumitrescu C E, Puzinauskas P V and Olcmen S 2008 Movable fiber probe for gas-phase laser-induced breakdown spectroscopy *Appl. Opt.* **47** G88
[33] Hang Y-H, Qiu Y, Zhou Y, Liu T, Zhu B, Liao K, Shi M-X and Xue F 2022 Effects of pulse energy ratios on plasma characteristics of dual-pulse fiber-optic laser-induced breakdown spectroscopy *Chin. Phys. B* **31** 024212
[34] Yuan M, Zeng Q, Wang J, Li W, Chen G, Li Z, Liu Y, Guo L, Li X and Yu H 2021 Rapid classification of steel via a modified support vector machine algorithm based on portable fiber-optic laser-induced breakdown spectroscopy *Opt. Eng.* **60** 124114
[35] Sankhe M L, Favre A, Sirven J-B, Bultel A, L'hermite D, Semerok A, Vartanian S and Grisolia C 2023 Development of fibered LIBS device for tokamak plasma facing components characterization *Fusion Eng. Des.* **197** 114077
[36] Rajavelu H, Vasa N J and Seshadri S 2022 Hollow-core optical fiber-based laser-induced breakdown spectroscopy technique for the elemental analysis of pulverized coal *Appl. Phys. A* **128** 868

Publ. Astron. Obs. Belgrade No. 103 (2024), 153 *Poster*
https://doi.org/10.69646/aob103p153

INFLUENCE OF THE ABLATION ANGLE CHANGE ON SPECTRAL LINE INTENSITIES IN LIBS EXPERIMENTS

IVAN TRAPARIĆ*, BILJANA STANKOV, NIKOLA VUJADINOVIĆ, MILICA VINIĆ and MILIVOJE IVKOVIĆ

Institute of Physics Belgrade, Pregrevica 118, 11080, Belgrade
**Corresponding author: traparic@ipb.ac.rs*

Abstract. Laser Induced Breakdown Spectroscopy - LIBS is the most promising technique for the in-situ analysis of the plasma fusion reactor walls, see (Cong Li at al, 2016). The setup which is most frequently used in fusion reactors is so-called remote in-situ RIS LIBS, see (Cai et al, 2019). This configuration uses a scanning system which controls the Mo mirror to direct the laser beam to a different position inside the fusion reactor. In this study, it was investigated how changes in the ablation angles affect the intensity of the emitted spectral lines, considering that the incident beam is not always perpendicular to the PFCs. To this end, the classical LIBS setup at atmospheric pressure was employed. The angle of collection fiber with respect to the laser beam was fixed to 17 degrees. Chosen targets were tungsten-based alloys relevant to fusion research. The spectrum of the plasma was recorded with a Solar MS7504i spectrometer and a fast camera. Results show that there is a non-trivial dependance of the line intensity on the ablation angles, which was attributed to the change of laser focus and ablation surface as the angles were varied both in poloidal and toroidal directions. Additionally, the line intensity correction factor was calculated as the ratio of the intensity for the beam incident at an angle to that of the beam at normal incidence, and it exhibited a complex dependence on both angles.

Acknowledgements
The research was funded by the Ministry of Education, Science and Technological Development of the Republic of Serbia, Contract number: 451-03-68/2022-14/200024, and supported by the Science Fund of the Republic Serbia, Grant no. 7753287.

References

Cong Li at al.: 2016, Front. Phys. **11**, 114214.
Laizhong Cai et al.: 2019, Rev. Sci. Instrum. **90**, 053503.

Contribution ID: **79** Type: **Poster**

Detection of hydrogen isotopes in fusion-relevant targets via laser ablation and microwave-induced plasma

Wednesday, 9 July 2025 14:40 (20 minutes)

Abstract. The analysis of plasma facing components (PFCs) of fusion machines using laser-induced breakdown spectroscopy (LIBS) technique is widely distributed in the fusion community. Difficulties arise when the spectroscopic measurements of tritium retention are performed, particularly the resolving of deuterium (Dα) and tritium (Tα) Balmer alpha lines becomes a major issue.
This study explores using microwave-induced plasma (MIP) generated in a custom-designed low-pressure chamber as a potential solution to this problem. The target material is introduced into the MIP via laser ablation using Nd:YAG laser, and the spectral signal is monitored with a high-resolution spectrometer and an ICCD camera. Two silicon-based targets were utilized: the first, coated with carbon (C) and methane (CH4), was used for optimization of the measurement system, whereas the second, coated with C and D, was used for final measurements.
As part of the optimization process, the optimal time window for signal recording was determined relative to the laser Q-switch trigger. Additionally, crater profiles were analyzed using an optical profilometer, yielding the estimated ablation rate of approximately 400 nm per laser pulse at a fluence of 5.4 J/cm^2.
The final measurements indicate that, with the current setup, the lowest detectable tritium level would correspond to a Tα line intensity between 30% and 50% of the Dα line intensity (Fig. 1). These results show that this MIP-based setup is a promising tool for such analyses, providing reliable and fast determination of tritium content retained in fusion-relevant materials.

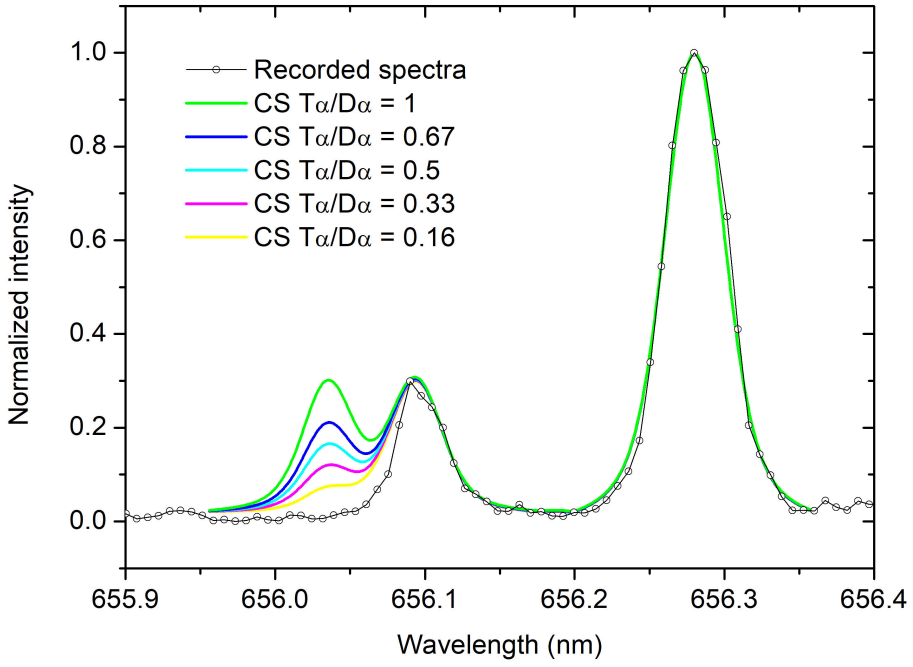

Figure 1: Figure 1. CS theory estimation of Tα resolving.

Author: VUJADINOVIĆ, Nikola (Institute of Physics, Belgrade)

Co-authors: Dr TRAPARIĆ, Ivan (Institute of Physics, Belgrade); Dr CIGANOVIĆ, Jovan (Vinca Institute of Nuclear Sciences, Belgrade); Dr ANGHEL, Alexandru (National Institute for Laser, Plasma and Radiation Physics, Bucharest); Dr POROSNICU, Corneliu (National Institute for Laser, Plasma and Radiation Physics, Bucharest); Dr IVKOVIĆ, Milivoje (Institute of Physics, Belgrade)

Presenters: VUJADINOVIĆ, Nikola (Institute of Physics, Belgrade); Dr TRAPARIĆ, Ivan (Institute of Physics, Belgrade)

Session Classification: Poster Session 1

Track Classification: S01 - Atomic, Molecular and Optical Physics